



Delft University of Technology

## Hydrogen, medium-range airplane design optimization for minimal global warming impact

Proesmans, P.; Vos, Roelof

**DOI**

[10.1007/s13272-024-00734-w](https://doi.org/10.1007/s13272-024-00734-w)

**Publication date**

2024

**Document Version**

Final published version

**Published in**

CEAS Aeronautical Journal

**Citation (APA)**

Proesmans, P., & Vos, R. (2024). Hydrogen, medium-range airplane design optimization for minimal global warming impact. *CEAS Aeronautical Journal*. <https://doi.org/10.1007/s13272-024-00734-w>

**Important note**

To cite this publication, please use the final published version (if applicable). Please check the document version above.

**Copyright**

Other than for strictly personal use, it is not permitted to download, forward or distribute the text or part of it, without the consent of the author(s) and/or copyright holder(s), unless the work is under an open content license such as Creative Commons.

**Takedown policy**

Please contact us and provide details if you believe this document breaches copyrights. We will remove access to the work immediately and investigate your claim.



# Hydrogen, medium-range airplane design optimization for minimal global warming impact

P. Proesmans<sup>1</sup> · Roelof Vos<sup>1</sup>

Received: 16 November 2023 / Revised: 16 November 2023 / Accepted: 4 March 2024  
© The Author(s) 2024

## Abstract

This paper focuses on the conceptual design optimization of liquid hydrogen aircraft and their performance in terms of climate impact, cash operating cost, and energy consumption. An automated, multidisciplinary design framework for kerosene-powered aircraft is extended to design liquid hydrogen-powered aircraft at a conceptual level. A hydrogen tank is integrated into the aft section of the fuselage, increasing the operating empty mass and wetted area. Furthermore, the gas model of the engine is adapted to account for the hydrogen combustion products. It is concluded that for medium-range, narrow-body aircraft using hydrogen technology, the climate impact can be minimized by flying at an altitude of 6.0 km at which contrails are eliminated and the impact due to  $\text{NO}_x$  emissions is expected to be small. However, this leads to a deteriorated cruise performance in terms of energy and operating cost due to the lower lift-to-drag ratio (– 11%) and lower engine overall efficiency (– 10%) compared to the energy-optimal solutions. Compared to cost-optimal kerosene aircraft, the average temperature response can be reduced by 73–99% by employing liquid hydrogen, depending on the design objective. However, this reduction in climate impact leads to an increase in cash operating cost of 28–39% when considering 2030 hydrogen price estimates. Nevertheless, an analysis of future kerosene and hydrogen prices shows that this cost difference can be significantly decreased beyond 2030.

**Keywords** Aircraft design · Hydrogen · Climate impact · MDO

## Abbreviations

ATR	Average temperature response [mK]
BPR	Bypass ratio
CG	Center of gravity
COC	Cash operating cost [USD]
far	Fuel-to-air ratio
GEOM	Geometry
GWP	Global warming potential
LHV	Lower heating value of fuel [MJ/kg]
LPC	Low-pressure compressor
HPC	High-pressure compressor
MAC	Mean aerodynamic chord
MLM	Maximum landing mass [kg]
MTOM	Maximum take-off mass [kg]
OEM	Operating empty mass [kg]
OPR	Overall pressure ratio

RF	Radiative forcing [ $\text{W}/\text{m}^2$ ]
RPK	Revenue passenger kilometer
SEC	Specific energy consumption [ $\text{MJ}/(\text{N s})$ ]
TET	Turbine entry temperature [K]
TLAR	Top-level aircraft requirement
TOP	Take-off parameter
TSFC	Thrust specific fuel consumption [ $\text{kg}/(\text{N s})$ ]
XDSM	Extended design structure matrix

## Latin symbols

$A$	Aspect ratio or cross-sectional area [– or $\text{m}^2$ ]
$b$	Wing span [m]
$c$	Climb rate [m/s]
$c_p$	Isobaric specific heat [ $\text{J}/(\text{kg K})$ ]
$C_L$	Lift coefficient [–]
$C_D$	Drag coefficient [–]
$C_{D_0}$	Zero-lift drag coefficient [–]
$C_{D_w}$	Wave drag coefficient [–]
$c_p$	Specific heat capacity at constant pressure [ $\text{J}/(\text{kg K})$ ]
$EI_i$	Emission index of species $i$ [ $\text{kg}/\text{kg}$ ]
$e$	Oswald factor [–]
$F$	Objective function [mK, USD, or MJ]

✉ P. Proesmans  
P.Proesmans@tudelft.nl

<sup>1</sup> Faculty of Aerospace Engineering, Delft University of Technology, Kluyverweg 1, Delft 2629 HS, The Netherlands

$h$	Altitude or specific enthalpy [m or J/kg]
$m$	Mass [kg]
$\dot{m}$	Mass flow [kg/s]
$M$	Mach number [–]
$M_i$	Molar mass of species $i$ [g/kmol]
$p$	Pressure [N/M <sup>2</sup> ]
$p^i$	Partial pressure of species $i$ [N/M <sup>2</sup> ]
$r$	Range [km]
$R$	Gas constant [J/(kg K)]
$R_h$	Range-equivalent fuel calorific value ( $R_h = \text{LHV}/g$ ) [J/(kg K)]
$S$	Wing surface area [m <sup>2</sup> ]
$T$	Thrust [kN] or temperature [K]
$t_{bl}$	Block time [h]
$U_{\text{ann}}$	Annual utilization [h/year]
$V$	Volume [m <sup>3</sup> ]
$\bar{V}$	Tail volume coefficient [–]
$v$	Velocity [m/s]
$W$	Weight [kN]
$\mathbf{x}$	Design vector

### Greek symbols

$\gamma$	Ratio of specific heats [–]
$\Delta T$	Surface temperature change [K]
$\eta_{\text{ov}}$	Overall propulsion efficiency [–]
$\eta_{\text{grav}}$	Gravimetric index [–]
$\Lambda_{0.25}$	Wing quarter-chord sweep angle [deg]
$\lambda$	Wing taper ratio [–]
$\rho$	Density [kg/m <sup>3</sup> ]
$\phi$	Temperature-dependent fraction of entropy [J/(kg K)]

### Sub- and superscripts

0	Sea-level condition or initial value
0.25	Measured at quarter-chord
amb	Ambient condition
app	Approach condition
cr	Cruise condition
eng	Engine
ht	Horizontal tail
L	Lower bound
TO	Take-off condition
U	Upper bound
vt	Vertical tail
*	Optimal solution

## 1 Introduction

Fossil fuels and the associated emissions are leading to an increased burden on the environment [18]. Among other sectors, commercial aviation undeniably performs a role in the combustion of these fuels and the related effects on the climate [24]. These effects do not only arise due to the

emission of carbon dioxide (CO<sub>2</sub>) but also the emission of nitrogen oxides (NO<sub>x</sub>) and contrail formation are important factors. With a continued and rapid growth in commercial aviation [1, 6], it is clear that an urgent transition to new technologies and operations is required to reduce the climate impact.

Previous studies have investigated the potential to reduce the global warming impact of kerosene aircraft through re-optimization of airframe, engine, and mission variables [4, 11, 15, 22, 35], including the application of new technologies and/or operational changes. It was shown that the objectives of operating cost, fuel mass, and climate impact are conflicting and that flying lower and slower is key to reduce the burden of non-CO<sub>2</sub> effects. Nevertheless, the climate impact reduction of kerosene aircraft, even at low altitudes, is limited by the unavoidable emissions of CO<sub>2</sub> causing long-term warming.

Hydrogen fuel can provide a more sustainable alternative if it is produced from sustainable energy sources. It eliminates the emissions of carbon dioxide, as well as sulfate and soot particles [12]. Acknowledging the remaining uncertainty, several research projects examined the potential climate impact reduction of hydrogen aircraft. Svensson et al. [43] estimated that the Global Warming Potential (GWP) of medium-range aircraft can be reduced by approximately 15% and that in particular, flying lower has a notable impact, since it prevents contrail formation. In research by Ponater et al. [33], three transition scenarios toward cryoplane technology are assessed. Here, it was concluded that, depending on the scenario, a decrease in surface temperature change of 5–15% is possible compared to the kerosene reference scenario.

Both studies considered the increase in water vapor (H<sub>2</sub>O) emissions, potential reduction in NO<sub>x</sub> discharge, and change in contrail properties, mainly optical depth and lifetime. The alteration of these contrail properties is caused by the lack of soot particles in the exhaust plume, as examined by Ström and Gierens [41]. From these insights, Marquart et al. [27] further analyzed the radiative effect of contrails and formed the conclusion that the decreased optical thickness can counteract the increased formation frequency due to increased water vapor emissions, although the net effect is still uncertain. More recently, Burkhardt et al. [8] further studied the relation between contrail radiative forcing and initial ice particle number.

Despite this opportunity for significant climate impact reduction, the integration of liquid hydrogen into the existing tube-and-wing concept and its operations does not come without hurdles. First of all, there is the need to store the liquid hydrogen in cryogenic tanks, which require a (near) cylindrical shape to efficiently deal with the pressure differential and the application of insulation material [20]. Furthermore, liquid hydrogen has a low volumetric

energy density (approximately  $8496 \text{ MJ/m}^3$  compared to  $34\,511 \text{ MJ/m}^3$  for kerosene [12]), and thus requires a noteworthy volume. These two aspects, shape and volume, practically eliminate the option of storing liquid hydrogen in the relatively thin, high-subsonic wings of commercial aircraft.

The impact of hydrogen propulsion and the associated tank fitment on aircraft characteristics and performance has been studied in several research projects. System and sub-system design and analysis of hydrogen aircraft are covered in the studies by Brewer [7]. Furthermore, extensive system analyses of hydrogen aircraft were performed in the CRYOPLANE project [51]. It was concluded that the overall energy consumption and the operating empty mass (OEM) of hydrogen aircraft are higher than the kerosene alternatives, while the net effect on the aircraft maximum take-off mass (MTOM) is dependent on the category. Especially, the ratio between OEM and MTOM increases, because the higher specific density of hydrogen allows reducing the fuel mass, while the structural mass of the airframe increases. Similar trends can be observed in the studies by Verstraete [48]. Although multiple integration options are available [12, 20, 31, 48], a comparison between them is considered out of scope for the current discussion.

Although much of the cited work investigates the impact of hydrogen on climate impact, research into the conceptual optimization of hydrogen-powered aircraft, with a holistic evaluation of the climate impact, energy consumption, and cost, appears to be missing. Rather than studying individual sub-systems of a hydrogen aircraft, this study examines the design of hydrogen aircraft for various objectives and compares these concepts with their kerosene alternatives. The aim is to understand whether the transition to hydrogen is viable and sustainable, paving the way toward further research into the sub-system design of hydrogen aircraft. To achieve this objective, two research questions are targeted in this paper. The first research question focuses on the optimization of hydrogen aircraft, namely: how do the aircraft design variables of a liquid-hydrogen aircraft change when shifting from a cost to a climate objective? And second, how do these liquid-hydrogen optimized solutions compare to a kerosene alternative in terms of cost, climate impact, and energy consumption?

The aircraft are to be designed for a fixed set of top-level aircraft requirements (TLARs), targeting the medium-range, narrow-body market. Contrary to many design studies, the cruise Mach number and cruise altitude are added to the design variables. The classic tube-and-wing configuration with turbofan engines is assumed in the present study. In the case of the hydrogen aircraft, a liquid hydrogen tank is positioned in the rear section of the fuselage. The focus of this paper lies primarily on the global warming impact, and less

on other environmental aspects such as noise and air quality. It is recognized that the introduction of hydrogen technology brings additional hurdles to overcome, especially in terms of safety and airport logistics [12]. Nonetheless, the potential impact of these considerations on the aircraft design is left for further research.

The paper adheres to the following structure: Sect. 2 outlines the optimization problem and discusses the multidisciplinary design and analysis framework. The verification of the hydrogen gas model is provided in Sect. 3. Section 4 presents the results of the optimization study and compares the two fuel alternatives, answering the research questions posed above. Since the conceptual approach includes several assumptions and uncertainties, an assessment thereof is made in Sect. 5. Finally, Sect. 6 presents the conclusions and provides suggestions for further research.

## 2 Optimization definition and methodology description

The research questions posed above are solved by employing multidisciplinary design optimization (MDO). For kerosene aircraft, such a framework is already in place [35]. In this study, the MDO routine is extended to design and analyze liquid hydrogen aircraft in a conceptual design stage. In this section, first, the optimization problem and MDO architecture are formulated. Second, the individual disciplines are elaborated in Sect. 2.2, with a focus on the modifications for the hydrogen-powered aircraft. Section 2.3 defines the fleet scenario which is considered in the optimizations.

### 2.1 Optimization problem formulation

Since earlier research indicated that the climate-optimal aircraft designs conflict with the cost and fuel burn objectives [11, 15, 22], the three objectives and the trade-offs between them have to be studied separately. In the current study, the three single objectives are the climate impact measured by the average temperature response ( $\text{ATR}_{100}$ ), cash operating cost (COC), and energy consumption ( $E_{\text{fuel}}$ ). The reason for selecting the energy consumption rather than the fuel mass is that directly comparing the fuel burn of kerosene aircraft to that of hydrogen aircraft is not fair due to the large difference in calorific value of the fuels. Nevertheless, setting the energy or fuel burn as an optimization objective does yield the same design, since the two objectives are linearly related by the respective calorific value. This yields the following optimization problem definition:

**Table 1** Design variables and their respective bounds

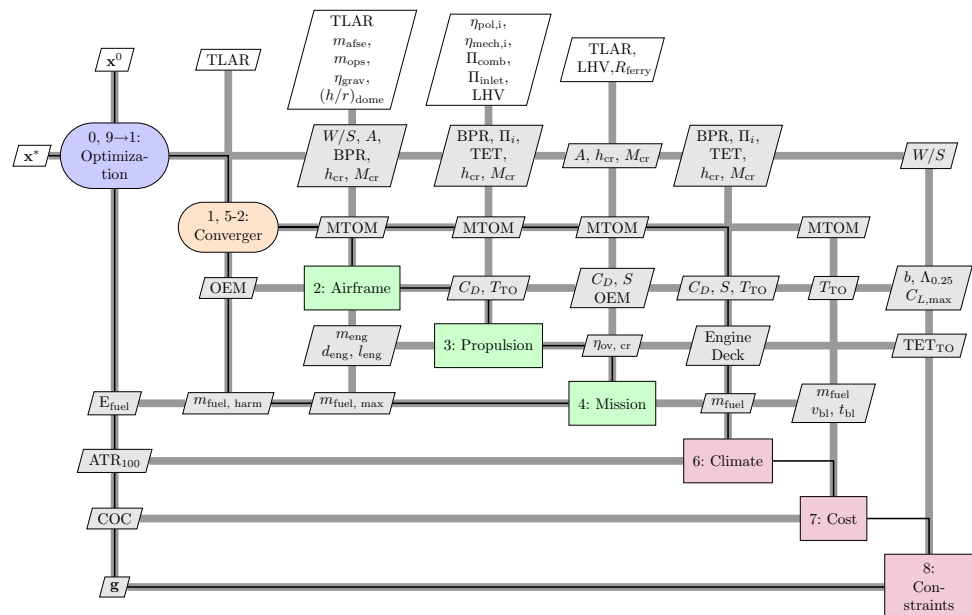
Variable	Description [Unit]	Lower bound ( $x^L$ )	Upper bound ( $x^U$ )
$W/S$	Wing loading [kN/m <sup>2</sup> ]	3.00	6.50
$A$	Aspect ratio [-]	7.00	12.0
BPR	Bypass ratio [-]	6.00	11.0
$\Pi_{fan}$	Fan pressure ratio [-]	1.30	1.80
$\Pi_{lpc}$	LPC pressure ratio [-]	1.20	1.80
$\Pi_{hpc}$	HPC pressure ratio [-]	15.0	25.0
TET	Turbine entry temperature [K]	1350	1700
$h_{cr}$	Initial cruise altitude [km]	6.00	12.0
$M_{cr}$	Cruise Mach number [-]	0.50	0.90

minimize  $F(\mathbf{x}) = ATR_{100}(\mathbf{x})$  or  $COC(\mathbf{x})$  or  $E_{fuel}(\mathbf{x})$   
 subject to  $W/S \leq \frac{1}{2} \rho_0 \left( \frac{v_{app}}{1.23} \right)^2 C_{L_{max}} f_W$ ,  
 $b \leq b_{max}$ ,  
 $TET_{TO} \leq TET_{TO, max}$ ,  
 $OPR \leq OPR_{max}$ ,  
 $\Pi_{fan, TO} \leq \Pi_{fan}^U$ ,  
 $\Pi_{LPC, TO} \leq \Pi_{LPC}^U$ ,  
 $\Pi_{HPC, TO} \leq \Pi_{HPC}^U$ ,  
 $C_{L_{cr}} \leq \frac{C_{L_{buffet}}}{1.3} = \frac{0.86 \cdot \cos \Lambda_{0.25}}{1.3}$ ,  
 $x_i^L \leq x_i \leq x_i^U$  for  $i = 1, 2, \dots, 9$ .

This problem aims to find the design vector  $\mathbf{x}$ , defined by the nine variables in Table 1, which minimizes one of these objectives or forms a Pareto-optimal point in the multi-objective case. The nine variables are divided into three categories. First, two variables are related to the airframe, being the aspect ratio ( $A$ ) and wing loading at take-off ( $W/S$ ). Second, five design variables define the turbofan engine design cycle at top-of-climb, namely the bypass ratio (BPR), pressure ratios of the fan, low-pressure compressor (LPC), high-pressure compressor (HPC), and the turbine entry temperature (TET). Finally, the initial cruise altitude ( $h_{cr}$ ) and the cruise Mach number ( $M_{cr}$ ) influence the mission profile. Table 1 also provides the upper and lower bounds employed in this study. These are selected based on current technological and operational limitations, while also considering the assumptions made in the conceptual methods.

The design space is confined by eight inequality constraints, denoted by  $\mathbf{g}$  in Fig. 1. The first constraint in Eq. (1) ensures that the selected wing loading is low enough to meet the minimum approach speed  $v_{app}$ , which is set to 70.0 m/s [2]. The value of the maximum lift coefficient ( $C_{L_{max}}$ ) is derived from the wing quarter-chord sweep, as discussed in Sect. 2.2.3. A correction is included to consider that the maximum approach mass is lower than the MTOM. To formulate the constraint for the wing loading at take-off, it is assumed that the maximum approach or landing mass is 12% ( $f_W = 1/0.88$ ) and 4% ( $f_W = 1/0.96$ ) lower than the take-off mass for the kerosene and hydrogen aircraft, respectively. The second constraint limits the wing span  $b$  to 36 m, which is the upper limit for aircraft belonging to the ICAO 4C category. Third, the maximum turbine entry temperature at take-off (ISA+15),

**Fig. 1** Extended design structure matrix showing the multidisciplinary design workflow adapted from [35] to design hydrogen aircraft. The data connections (gray parallelograms) between the design and analysis modules (green boxes) and function evaluations (red boxes) are indicated by the wide, gray lines. The black line defines the computational execution order



$TET_{TO, \max}$ , is restricted to 2000 K according to Mattingly et al. [29]. The fourth constraint limits the overall pressure ratio (OPR) at top-of-climb to 60. Additionally, the pressure ratios of the fan, low-pressure compressor, and high-pressure compressor in take-off are also constrained by the upper boundaries set in Table 1. The final constraint prevents the aircraft lift coefficient in cruise from reaching the buffet onset condition. The regulations stipulate that the maximum lift coefficient achieved at any point in flight should be 30% lower than the one at which buffet occurs. The relation is derived from the buffet onset boundaries collected by Obert [30].

The extended design structure matrix (XDSM) in Fig. 1 presents how the disciplines are connected, which data are shared between them, and the computational order of execution. At the core of the framework is the convergence loop which produces consistent aircraft designs in terms of mass for a design vector provided by the optimization module and a fixed set of TLARs. For each aircraft design, the climate impact, operating cost, and constraints are evaluated (steps 6–8) to update the design vector. The airframe and propulsion modules consist of subroutines, as displayed in Figs. 2 and 3. Although the XDSM in Fig. 1 is similar for both aircraft types, the individual disciplines differ. Appendix A provides further details about the optimization algorithm and presents the convergence in Figs. 14 and 15.

In the optimizations, we only consider the in-flight energy consumption and the climate impact due to in-flight emissions. For a complete overview, one should also consider the energy needed to produce the fuels and the resulting climate impact. This requires a full life-cycle assessment. Such an analysis is quite elaborate and would add more uncertainty to the current MDO approach. Therefore, the life-cycle assessment is outside the scope of this paper.

## 2.2 Design and analysis methods

The following sections discuss the design and analysis steps taken in the individual disciplines. Since the modules of an existing aircraft design framework are extended [35], the sections focus on the changes made for the integration of liquid hydrogen.

### 2.2.1 Class-I sizing

The Class-I sizing module aims to compute the wing surface area ( $S$ ) and the sea-level take-off thrust ( $T_{TO}$ ), which influence geometry creation, mass estimation, and propulsion-system design. The surface area can be computed from the wing loading and the MTOM estimate in the current design loop.  $T_{TO}$  follows from the sea-level, thrust-to-weight ratio, which is selected, such that it is the minimum value

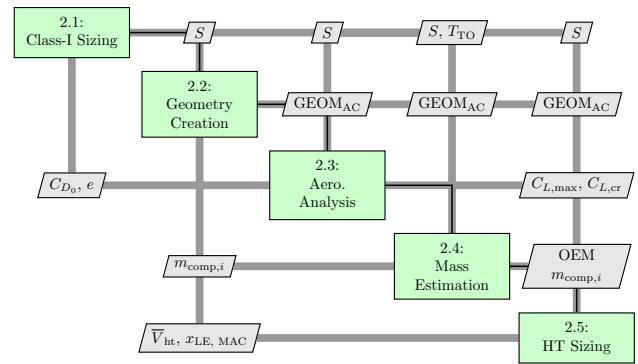


Fig. 2 Airframe design and analysis workflow (step 2 in Fig. 1)

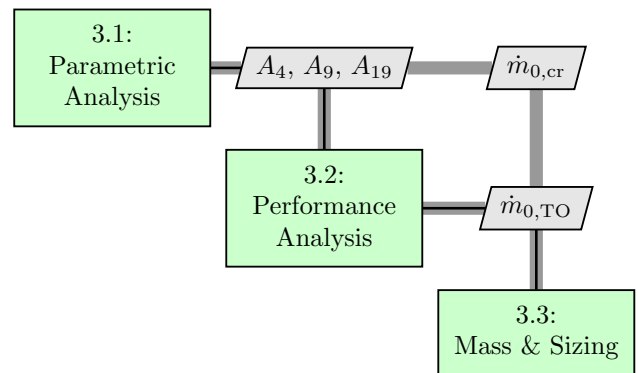


Fig. 3 Propulsion design and analysis workflow (step 3 in Fig. 1) [35]

satisfying all six imposed performance constraints. This is mathematically expressed by the following equation, which is directly dependent on the design variables  $W/S$ ,  $A$ , and  $M_{cr}$ , and indirectly on  $h_{cr}$ :

$$\frac{T_{TO}}{W} = \max \left\{ \frac{W/S}{TOP} \cdot \frac{1}{C_{L_{TO}}}, \frac{T_{TO}}{T_{cr}} \left( \frac{\rho_0}{\rho_{cr}} \right)^{\frac{3}{4}} \left[ \frac{C_{D_{0, cr}} \frac{1}{2} \gamma p_{cr} M_{cr}^2}{(W/S)_{cr}} + \frac{(W/S)_{cr}}{\pi A e_{cr} \frac{1}{2} p_{cr} \gamma M_{cr}^2} \right], \left[ \frac{c}{v} \right]_{TO, N_{eng}} + 2 \sqrt{\frac{C_{D_{0, TO}}}{\pi A e_{TO}}}, \left[ \frac{c}{v} \right]_{app, N_{eng}} + 2 \sqrt{\frac{C_{D_{0, app}}}{\pi A e_{app}}}, \frac{N_{eng}}{N_{eng} - 1} \left( \left[ \frac{c}{v} \right]_{TO, N_{eng} - 1} + 2 \sqrt{\frac{C_{D_{0, TO}}}{\pi A e_{TO}}} \right), \frac{N_{eng}}{N_{eng} - 1} \left( \left[ \frac{c}{v} \right]_{app, N_{eng} - 1} + 2 \sqrt{\frac{C_{D_{0, app}}}{\pi A e_{app}}} \right) \right\}. \quad (2)$$

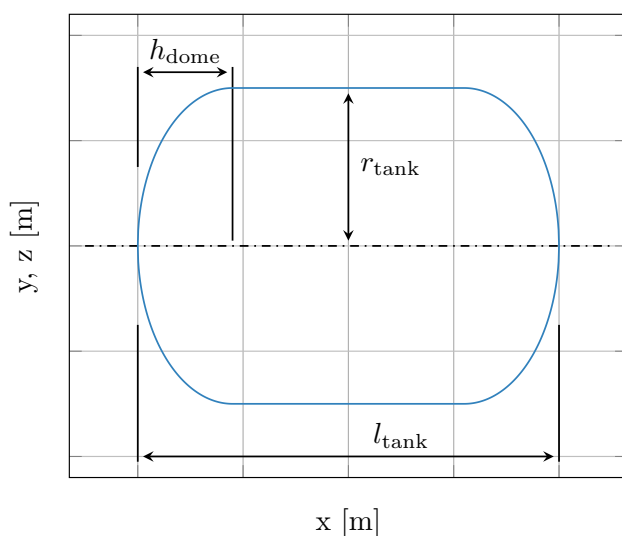
The first component within the curly brackets ensures that the required take-off length can be achieved, while the second component verifies that enough thrust is available in cruise conditions. These two constraints are set up according

**Table 2** Climb gradients ( $c/v$ ) to be met according to regulations

	Take-off	Approach or Landing
All engines operating ( $N_{\text{eng}}$ )	0.012 (CS25.111)	0.032 (CS25.119)
One engine inoperative ( $N_{\text{eng}} - 1$ )	0.024 (CS25.121)	0.021 (CS25.121)

to previously discussed methods [35, 36], where the density  $\rho$  and pressure  $p$  are altitude-dependent and calculated through the International Standard Atmosphere (ISA) model. The take-off length for the medium-range case study is presented in Table 4 along with other top-level requirements. The wing loading at the start of cruise is considered to be lower due to fuel consumed during take-off and climb. The next four components guarantee that the thrust level is sufficient to produce the required climb gradient ( $c/v$ ) in several all-engines-operating conditions and one-engine-inoperative situations. The subscripts “TO”, “cr”, and “app” refer to the configuration of the aircraft is in take-off, cruise, or approach, respectively. The zero-lift drag coefficients ( $C_{D_0}$ ) and Oswald factors ( $e$ ) are adapted to the applicable configuration. Table 2 provides the minimum climb gradients to be achieved in these four situations and references to the respective regulations.

These performance requirements are only considered in the Class-I sizing module and are not constraints in overall multidisciplinary optimization. This approach ensures that every design solution coming from the synthesis loop automatically meets these requirements. In addition, this eliminates  $T_{\text{TO}}$  as a design variable in the overall optimization. However, depending on the selected wing loading and aspect ratio, different requirements may become active. Such a disruptive change

**Fig. 4** Longitudinal section of the liquid hydrogen tank concept

can cause problems when a gradient-based optimization algorithm is used. To overcome this issue, a multi-strategy approach is used when solving the optimization problem. We discuss this approach in more detail in Appendix A.

## 2.2.2 Geometry creation

The aircraft geometry is required to determine the drag polar in module 2.3 (Sect. 2.2.3) and to predict the structural mass in module 2.4 (Sect. 2.2.4). The creation is fully automated to facilitate the MDO. This automation is achieved through statistical relationships and assumptions based on existing medium-range, narrow-body aircraft concepts such as the Airbus A320 and Boeing 737 [2, 5].

The wing is sized according to the surface area, retrieved from the analysis in Sect. 2.2.1, the aspect ratio, the cruise Mach number, and the lift coefficient. The span is determined directly from  $S$  and  $A$ , while the remainder of the planform is defined by the quarter-chord sweep angle and the taper ratio, which are determined from the cruise Mach number and data of high-subsonic and transonic aircraft [19, 46]. The cruise lift coefficient provides an estimate of the airfoil thickness-to-chord ratio, which in turn is employed in the aerodynamic analysis and mass estimation.

Different from the wing geometry, the fuselage geometry is dependent on the fuel type. For the kerosene-powered aircraft, the fuselage consists of three sections: the cockpit, cabin, and tail. First, the inner and outer diameters are computed based on the number of seats abreast in the cabin and the LD3-45 unit load device in the cargo bay below. For the current study, a six-abreast, single-aisle configuration is selected, leading to inner and outer diameters of approximately 3.91 and 4.06 m, respectively. A maximum capacity of 180 passengers thus results in a cabin consisting of 30 rows and being approximately 27 m long. This maximum capacity is arranged in a single-class configuration, which is taken to be the sizing configuration for the cabin. Two- or three-class configurations can be fitted, albeit at a lower passenger number. This cabin layout is similar to the ones of the Airbus A320 [2] and Boeing 737-900 [5]. The cockpit is assumed to be 4 m long and the length of the tail section is 1.6 times the outer diameter.

For the hydrogen aircraft, a cylindrical, cryogenic tank is integrated into the aircraft. Although various integration solutions exist [12, 31], in this study, the tank is positioned aft of the cabin in the fuselage in a non-integral manner. This is a rather straightforward solution for the aircraft category under investigation, since it results in a relatively short tank and does not interrupt the conventional connection between the cockpit and the cabin. The maximum fuel mass ( $m_{\text{fuel,max}}$ ), together with the density of liquid hydrogen ( $71 \text{ kg/m}^3$ ), provides an estimate for the maximum tank

volume ( $V_{\text{tank}}$ ). Assuming the tank diameter ( $d_{\text{tank}} = 2r_{\text{tank}}$ ) is equal to the inner diameter of the fuselage and the end caps of the tank are ellipsoids, the tank length can be determined as follows:

$$l_{\text{tank}} = \frac{1}{\pi r_{\text{tank}}^2} \left[ V_{\text{tank}} - \frac{4\pi}{3} \cdot r_{\text{tank}}^2 \cdot h_{\text{dome}} \right] + 2h_{\text{dome}}$$

where  $h_{\text{dome}} = r_{\text{tank}} \cdot \left( \frac{h}{r} \right)_{\text{dome}}$  and (3)

$$V_{\text{tank}} = \frac{m_{\text{fuel,max}}}{\rho_{\text{LH}_2}} \cdot (1 + f_{V,\text{extra}}).$$

Figure 4 displays a conceptual longitudinal section of the tank model with the dimensions from the relation above. The ratio between the dome height and the tank radius  $(h/r)_{\text{dome}}$  is selected as the control variable, since it facilitates scaling the domes automatically with the radius, and because its value lies in the interval between zero and one. Although this ratio only influences the total tank length, it does not influence the mass of the tank itself in the current model. Lower values of  $(h/r)_{\text{dome}}$  can reduce the fuselage mass, but any penalty on stress levels due to the internal pressure is not accounted for. In the optimizations, the ratio is set to 0.3. The sensitivities of aircraft-level parameters to this assumption are discussed in Sect. 5.1.

The tank outer diameter is assumed to be equal to the inner diameter of the fuselage, which is equal to the diameter of the cabin. This leaves approximately 15 cm around the tank for insulation material and structural components. In this approximation, the volume of the tank is determined from the maximum amount of liquid hydrogen it has to hold, plus extra allowances to account for contraction and expansion (0.9%), ullage (2%), internal equipment (0.6%), and trapped fuel (0.3%) [7, 31]. These allowances are captured by the factor  $f_{V,\text{extra}}$  in Eq. (3). However, we do not allocate volume for boil-off resulting from heat leakage into the tank. The effect of this assumption on the optimization objectives and key performance indicators is quantified in Sect. 5.1

The longitudinal location of the main wing and the size of the horizontal tail surface are determined by considering the aircraft mass balance and the longitudinal stability and trim conditions [46]. The design routine computes the in-flight center-of-gravity (CG) excursion over the mean aerodynamic chord (MAC) as a function of the longitudinal wing position. Simultaneously, the stability constraints in cruise conditions and the trim conditions in approach (full flaps deployed) are assessed. These constraints provide an estimate of the horizontal tail size area with respect to the reference wing area ( $S_{\text{ht}}/S$ ), for a given CG excursion. An internal optimization finds the wing position which minimizes the horizontal tail area, adhering to the imposed stability and trim constraints.

We determine the mass balance and CG excursion by first calculating the CG position corresponding to the

OEM. This step considers the relative, structural mass fractions of fuselage group components (fuselage, empennage, and in the case of the hydrogen aircraft, the tank) and the wing group elements (wing and engines) and their relative positions. While the relative mass fractions for the kerosene concept can be taken from literature, these data are not available for hydrogen aircraft. Therefore, these mass fractions are updated throughout the iterations, as can be seen in Fig. 2 where the mass estimation module feeds the component masses  $m_{\text{comp},i}$  back to the geometry module. Subsequently, the passengers and fuel are loaded, taking into account several loading scenarios: passenger loading from the front and back, full and empty fuel tank, and the ferry mission with full fuel tank and no passengers. This process finds the largest, critical, in-flight CG excursion, which sizes the horizontal tail.

Compared to the kerosene aircraft, the liquid hydrogen counterpart with a tank in the aft fuselage section features a longer tail arm, but also a larger CG excursion. Additionally, the stability constraint is updated according to the increase in fuselage length. The net effect is that for the same top-level requirements, the liquid hydrogen aircraft will have a larger horizontal tail size. This increases the OEM and increases the zero-lift drag, negatively influencing energy consumption.

The size of the vertical tail is determined through a fixed volume coefficient ( $\bar{V}_{\text{vt}}=0.085$ ), based on statistical data [36]. A physics-based sizing approach to the vertical tail is considered outside the scope of the current study, since such analysis would require more knowledge about the design. Nevertheless, the effect of the longer fuselage, among other effects, on the vertical tail area should be evaluated, taking into account lateral and directional stability constraints in various conditions, including one-engine-inoperative and cross-wind situations.

The aspect ratios and taper ratios of the horizontal and vertical tails are taken from literature and are assumed to be equal for the kerosene and hydrogen aircraft. These values are summarized in Table 3. The quarter-chord sweep angle of the horizontal and vertical stabilizers is 3 and 10 degrees, respectively, more than the main wing quarter-chord sweep angle.

### 2.2.3 Aerodynamic analysis

The aerodynamic module provides an estimation of the aircraft drag polar based on the external shape and size of the aircraft. The propulsion, mission, and Class-I sizing modules require this drag polar to size the propulsion system, evaluate the fuel burn, and evaluate the performance constraints in Eq. (2). In this study, a quadratic drag polar is assumed according to the following formula:



**Table 3** Fixed design parameters for horizontal and vertical tail surfaces

Parameter [Unit]	Value
Horizontal tail aspect ratio $A_{ht}$ [-]	5.0
Vertical tail aspect ratio $A_{vt}$ [-]	1.7
Horizontal tail taper ratio $\lambda_{ht}$ [-]	0.4
Vertical tail taper ratio $\lambda_{vt}$ [-]	0.6

$$C_D = C_{D_0} + \frac{C_L^2}{1.05\pi Ae} + C_{D_w}, \tag{4}$$

where  $C_{D_0}$  is the zero-lift drag coefficient,  $A$  is the aspect ratio,  $e$  is the Oswald factor, and  $C_{D_w}$  is the wave drag coefficient. The zero-lift drag is computed as the sum of the minimum profile drag of all components (wing, fuselage, nacelles, and empennage) and the drag contributions due to excrescences or protuberances [30, 35], such as antennas and door intersections. The Oswald factor is determined from a statistical relation involving the design variable  $A$  [35]. The 5% increase in the product  $A \cdot e$  is included to model the influence of wing tip devices that do not contribute to the wing span. This contribution is derived from the Airbus A320 winglet span.

Equation (4) provides an estimate of the drag coefficient in clean configuration (i.e., with all flaps and landing gear retracted). To correct this estimation in landing and take-off settings, constant terms are added to  $C_{D_0}$  and  $e$  [35, 36]. Based on data provided by Roskam [36], the zero-lift drag is increased by 0.015 and 0.085 in take-off and landing configuration, respectively. The contributions of the flaps to  $e$  are assumed to be equal to 0.05 and 0.10 during take-off and landing, respectively.

The last term in the drag polar equation accounts for the wave drag. This term accounts for transonic flow around the aircraft, an increase in drag when shocks are formed. In this approach, we only consider the wave drag of the wing [32]. The wave drag component is computed using the following equation according to the methods introduced by References [28, 32]:

$$C_{D_w} = \begin{cases} 0 & \text{if } M_{cr} \leq M_{dd} - \left(\frac{0.1}{80}\right)^{1/3} \\ 20 \cdot \left[ M_{cr} - M_{dd} + \left(\frac{0.1}{80}\right)^{1/3} \right]^4 & \text{if } M_{cr} > M_{dd} - \left(\frac{0.1}{80}\right)^{1/3} \end{cases}, \tag{5}$$

where  $M_{dd}$  is the drag divergence Mach number at which the drag rise is 0.1 (i.e.,  $\partial C_D / \partial M = 0.1$ ). This Mach number is determined as follows:

$$M_{dd} = \frac{k_a}{\cos(\Lambda_{0.25})} - \frac{t/c}{\cos^2(\Lambda_{0.25})} - \frac{C_{l,crit}}{10 \cos^3(\Lambda_{0.25})}, \tag{6}$$

where we assume a value of 0.935 for the airfoil technology factor  $k_a$ . The parameter  $C_{l,crit}$  is the local critical lift coefficient, which is presumed to be equal to the wing lift coefficient divided by 0.9.  $t/c$  is the averaged thickness-to-chord ratio. This parameter and the quarter-chord sweep angle are determined from statistical relations [35] to minimize the wave drag at high subsonic conditions. When the design cruise Mach number increases and  $t/c$  reaches the lower limit of 0.10, the wave drag starts to increase more rapidly with the design Mach number.

The maximum lift coefficient of an aircraft, defined in the configuration with all high-lift devices fully deployed, is conceptually a function of the wing sweep angle and the type of flap system. Since the cruise Mach number drives the wing sweep, this design variable also limits the maximum achievable lift coefficient. In the conceptual framework, this reasoning is included through the following equality [30]:

$$C_{L_{max}} = 2.8 \cdot \cos \Lambda_{0.25}. \tag{7}$$

### 2.2.4 Mass estimation

The convergence loop at the core of the optimization framework ensures that the aircraft evaluated in the climate and cost modules is consistent in terms of mass and geometry. A key parameter in this convergence is the maximum take-off mass, which is the sum of the payload mass, fuel mass, and operating empty mass. While the first component is a top-level aircraft requirement and the fuel mass follows from the mission analysis, the OEM has to be computed based on the aircraft configuration and expected loads. Especially in the case of hydrogen aircraft, the influence of the fuel tank on the OEM has to be taken into account.

In the current study, the Class-II methods introduced by Torenbeek [46] provide the necessary update of the OEM, albeit with adaptations for the hydrogen alternative. Although this reference does not provide any specialized methodology to size the hydrogen tank, the majority of the relations are expected to be valid, because they allow the analysis of configurations with a kerosene tank in the aft fuselage section. The main changes to the methodology occur in the estimation of fuselage mass, wing mass, tank mass, the mass of operational items, and airframe equipment mass.

The first alteration is the elongation of the fuselage due to the integration of the hydrogen tank aft of the cabin, as discussed in Sect. 2.2.2. The structural fuselage mass estimation depends largely on the skin area, which automatically increases with the length of the fuselage. The

mass also scales with the cabin floor area. While in the conventional aircraft, this floor runs up to the tail section, in the case of the hydrogen aircraft this floor stops in front of the fuel tank. Hence, the floor area is approximately equal for both aircraft types, since the passenger requirements remain unaltered.

The analysis of the wing mass remains similar, with the main difference being the mass for which the wing is designed. The method from Reference [46] requires the maximum aircraft mass with zero fuel in the wings. For kerosene aircraft, this can be set equal to the maximum zero-fuel mass (MZFM), while for the hydrogen concept, the MTOM is expected to deliver more accurate results, since there is no fuel in the wings and thus no load alleviation.

In the existing framework, the mass of the operational items ( $m_{ops}$ ) and airframe services and equipment ( $m_{afse}$ ) are set to a fixed percentage of the MTOM. Nevertheless, these masses should not differ between the kerosene and hydrogen alternatives since the cabin layout and passenger services are unaltered. Therefore, it is decided to keep these masses constant for both aircraft types throughout the optimizations, as can be seen in the input block above the airframe step in Fig. 1. The mass of the operational items and fixed equipment are set to approximately 4770 kg and 8800 kg, respectively.

For the kerosene aircraft, the tank mass is included in the wing mass estimation. However, for the hydrogen aircraft, an additional component has to be added to account for the heavier, cryogenic tanks. A conceptual approach is taken where the tank mass scales with the maximum fuel mass it can hold, using the definition of the gravimetric index or efficiency [49]

$$\eta_{grav} = \frac{m_{fuel}}{m_{fuel} + m_{tank}}. \quad (8)$$

Note that in Reference [31],  $\eta_{grav}$  is defined differently, namely as the ratio between the tank mass and the fuel mass. Although this results in different values for  $\eta_{grav}$ , the tank and fuel mass ratios are similar among research projects [31]. The value of the gravimetric index varies depending on the tank design, but for a medium-range, narrow-body aircraft the value of 0.773 (0.294 in Reference [31]) is selected based on previous designs in the literature [31, 49] and kept constant throughout the optimizations. This allows the computation of the tank mass once the maximum fuel mass is known. The latter parameter is calculated in the mission analysis step from the desired ferry range. The influence of potential tank design options, such as venting pressure, tank shape, position, or insulation materials, is not examined in this research. However, Sect. 5.1 discusses the effect of the selected gravimetric index on the objective functions.

## 2.2.5 Propulsion

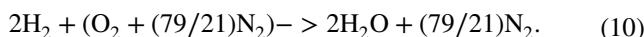
Based on the five engine design variables defined in Table 1, the thrust-to-weight ratio in take-off, and the drag polar, a preliminary turbofan is thermodynamically designed and sized. Both the kerosene- and hydrogen-powered aircraft utilize a two-spool turbofan engine with separate exhausts. This thermodynamic model is required to estimate the fuel burn and emissions throughout the flight in steps 4 and 6 of the XDSM in Fig. 1, while the engine size and mass are employed to update the drag polar and OEM in step 2.

Based on the cruise conditions, the thermodynamic cycle is determined by the parametric analysis module of Fig. 3. Subsequently, an off-design analysis is performed to find the required fuel flow for a given thrust at key points in the mission. Both the on-design and off-design point analyses are executed employing the strategies laid out by Mattingly et al. [29], and the variable specific heat model introduced by Walsh and Fletcher [50].

In the case of hydrogen combustion, two changes are implemented in the thermodynamic model of the turbofan engine. First of all, when replacing kerosene with hydrogen, the lower heating value (LHV) increases from 43.6 MJ/kg to approximately 120 MJ/kg. Second, since the composition of the combustion gases changes, characterized by the lack of carbon dioxide and increased water vapor content, the variable gas model is adapted. In particular, the values for the specific heat at constant pressure ( $c_p$ ), the specific enthalpy ( $h$ ), and the temperature-dependent fraction of entropy ( $\phi$ ) as functions of temperature are modified. The new relations, applicable through the turbines and the exhaust, are derived as follows:

$$\begin{aligned} c_p(T) &= f_{H_2O} \cdot c_{p,H_2O}(T) + f_{N_2} \cdot c_{p,N_2}(T) + f_{air} \cdot c_{p,air}(T) \\ h(T) &= f_{H_2O} \cdot h_{H_2O}(T) + f_{N_2} \cdot h_{N_2}(T) + f_{air} \cdot h_{air}(T) \\ \phi(T) &= f_{H_2O} \cdot \phi_{H_2O}(T) + f_{N_2} \cdot \phi_{N_2}(T) + f_{air} \cdot \phi_{air}(T) \\ R &= f_{H_2O} \cdot R_{H_2O} + f_{N_2} \cdot R_{N_2} + f_{air} \cdot R_{air}, \end{aligned} \quad (9)$$

where the  $f_i$  factors represent the fractions between the mass flow of compound  $i$  and the total core mass flow aft of the combustion chamber. These fractions follow from the simplified chemical equilibrium of hydrogen combustion and the fuel-to-air ratio,  $far = \dot{m}_{H_2} / \dot{m}_{air,in}$ , where  $\dot{m}_{air,in}$  is the air mass flow at the inlet of the combustor. Assuming the air at the inlet of the combustor consists purely of oxygen and nitrogen, the following simplified chemical reaction occurs:



From this reaction, the approximate stoichiometric fuel-to-air ratio can be computed

$$\left. \frac{\dot{m}_f}{\dot{m}_{air}} \right|_{st} = \frac{2 \cdot M_{H_2}}{M_{O_2} + \frac{79}{21} M_{N_2}} \approx 0.029, \tag{11}$$

where  $M_{H_2}$ ,  $M_{O_2}$ , and  $M_{N_2}$  are the molar masses of hydrogen, oxygen, and nitrogen, respectively. The fractions  $f_i$  in Eq. (9) can be determined by considering a mass balance over the combustor

$$\dot{m}_{in} = \dot{m}_{out} \Rightarrow \dot{m}_{air,in} + \dot{m}_{H_2} = \dot{m}_{H_2O} + \dot{m}_{N_2} + \dot{m}_{air,out}, \tag{12}$$

leading to

$$\begin{aligned} f_{H_2O} &= \frac{\dot{m}_{H_2O}}{\dot{m}_{out}} = \frac{M_{H_2O}}{M_{H_2}} \cdot \frac{\dot{m}_{H_2}}{(1 + far) \cdot \dot{m}_{air,in}} \\ &= \frac{M_{H_2O}}{M_{H_2}} \cdot \frac{far \cdot \dot{m}_{air,in}}{(1 + far) \cdot \dot{m}_{air,in}} \approx 8.94 \cdot \frac{far}{(1 + far)}, \end{aligned} \tag{13}$$

$$\begin{aligned} f_{N_2} &= \frac{\dot{m}_{N_2}}{\dot{m}_{out}} = \left(\frac{79}{21}\right) \frac{M_{N_2}}{2M_{H_2}} \cdot \frac{\dot{m}_{H_2}}{(1 + far) \cdot \dot{m}_{air,in}} \\ &= \left(\frac{79}{21}\right) \frac{M_{N_2}}{2M_{H_2}} \cdot \frac{far \cdot \dot{m}_{air,in}}{(1 + far) \cdot \dot{m}_{air,in}} \approx 26.13 \cdot \frac{far}{(1 + far)}, \end{aligned} \tag{14}$$

$$\begin{aligned} f_{air} &= \frac{\dot{m}_{air,out}}{\dot{m}_{out}} = \frac{\dot{m}_{air,in} - \dot{m}_{H_2} \cdot \left(\left. \frac{\dot{m}_f}{\dot{m}_{air}} \right|_{st}\right)^{-1}}{(1 + far) \cdot \dot{m}_{air,in}} \\ &= \frac{\dot{m}_{air,in} - far \cdot \dot{m}_{air,in} \cdot \left(\left. \frac{\dot{m}_f}{\dot{m}_{air}} \right|_{st}\right)^{-1}}{(1 + far) \cdot \dot{m}_{air,in}} \\ &\approx \frac{1 - 34.48 \cdot far}{1 + far}. \end{aligned} \tag{15}$$

The value of far is not the same as the stoichiometric fuel-to-air ratio as not all core airflow entering the combustor takes part in the combustion process. Together with the gas model relations of water, nitrogen, and air provided by Walsh and Fletcher [50], these fractions define the gas model aft of the combustor according to Eq. (9). The verification of this gas model is discussed in Sect. 3.

Additional assumptions are made to simplify the thermodynamic modeling, including constant component efficiencies, no cooling flows, and no power or bleed air offtake. The validity of these assumptions is tested and discussed in earlier research [35]. Furthermore, in the case of liquid hydrogen, the fuel may have to be heated prior to combustion, which may be done through a heat exchanger or by cooling the turbines. However, this latter aspect is considered out of scope in the current conceptual study.

The relation for the mass of the engines is assumed to be the same for both the kerosene and hydrogen engines but does take into account the mass variation due to bypass ratio, overall pressure ratio, and ingested mass flow [13,

35]. Although the hydrogen turbofan may feature a heat exchanger to gasify the liquid hydrogen, the combustion chamber can be made shorter due to the reduced residence time [34, 42]. The impact of these changes on the engine mass is not accounted for.

### 2.2.6 Mission analysis

The aim of the mission analysis in the framework of Fig. 1 is primarily to provide an update of the required fuel mass at the harmonic design point (i.e., the maximum achievable range at maximum structural payload), such that the MTOM can be updated in the convergence loop. Second, it also calculates the maximum fuel mass to fulfill the ferry range ( $r_{ferry}$ ) requirement. Although kerosene aircraft often have enough storage volume in the wings, the volume required to store the maximum amount of hydrogen fuel is critical in sizing the tank, and subsequently the fuselage and wing.

The assumed mission profile is displayed schematically in Fig. 5 and features, besides the nominal climb and cruise phases (2 and 3 in Fig. 5), also diversion and loiter phases (phases 5 to 8 in Fig. 5). We select a conservative diversion range of 250 nmi suitable for long-range missions. A total loiter time of 35 min at 457 m (1500 ft) is taken, corresponding to 30 min of final reserve fuel and 5 min of contingency fuel. This fuel policy is set up according to the Easy Access Rules for Air Operations provided by the European Union Aviation Safety Agency (EASA), in particular in Section AMC1.CAT.OP.MPA.150(b).

The mission fuel mass is estimated through the lost-range method introduced by Torenbeek [45]. This method calculates the ratio between the fuel and total take-off masses as a function of cruise range, propulsion efficiency, and lift-to-drag ratio, and applies corrections to account for take-off, climb, and maneuvering phases [35]. The method can be adapted for hydrogen by implementing the correct LHV in the calculation of  $R_H$ , the range-equivalent calorific value. Since the statistical estimates for the diversion and loiter phases, as indicated in Fig. 5, do not uphold for hydrogen aircraft, the estimates are replaced by the respective Breguet equations. Furthermore, the hydrogen fuel mass required for

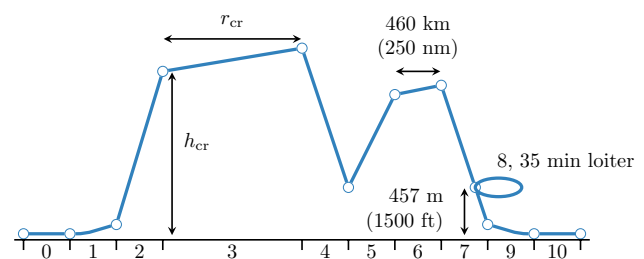


Fig. 5 Studied mission profile (flown distance versus altitude), adapted from [35]

maneuvers in the lost-range method is scaled by the lower heating value as follows:

$$\left(\frac{m_f}{m_{TO}}\right)_{\text{maneuver, LH2}} = \frac{0.0025}{\eta_{\text{ov}}} \cdot \frac{\text{LHV}_{\text{ker}}}{\text{LHV}_{\text{LH2}}}. \quad (16)$$

The lost-range method does not suffice for the climate impact evaluation, since the climate impact of  $\text{NO}_x$  emissions and contrail formation are dependent on engine off-design performance and altitude. Therefore, a separate mission analysis is performed during the climate impact evaluation which employs simplified flight mechanics and numerical integration. This mission analysis is computationally more expensive and is therefore not evaluated during the aircraft synthesis iterations to save time.

A comparison of the fuel mass estimates obtained from the two methods shows that the lost-range method marginally overpredicts the mission fuel mass. The lost-range method results in a 1–4% larger mission fuel mass, without the reserve mission phases, for both the kerosene and hydrogen aircraft. If we consider the detailed mission analysis to be a more accurate representation of reality, this overprediction in the aircraft design loop leads to heavier aircraft due to the snowball effect. This in turn increases the climate effects which scale with fuel burn. Nevertheless, since the excess fuel mass is limited to 4%, the overestimation of MTOM is smaller. Therefore, we expect that the overall penalty, introduced by the use of two different methods, is limited.

### 2.2.7 Global warming impact evaluation

Once the evaluation of the previous disciplines has yielded a consistent aircraft design, a climate impact and cost assessment of the concept can be made. Based on these assessments, the optimizer defines a new design vector to march toward the optimal design. This study combines the climate effects of several climate agents, including carbon dioxide, nitrogen oxides, contrails, water, and aerosols, into one comprehensive metric, namely the average temperature response over a period of  $H$  years, defined as follows:

$$\text{ATR}_H = \frac{1}{H} \int_0^H \Delta T(t) dt, \quad (17)$$

where  $\Delta T(t)$  is global mean surface temperature response in year  $t$ . This metric is computed for a hypothetical, future operations scenario which is further elaborated in Sect. 2.3. A period  $H$  of 100 years is selected to have a balanced assessment of long- and short-term effects.  $\Delta T(t)$  is computed through a linear temperature response model which, for kerosene aircraft, is described in Reference [35] and based on the model provided by Schwartz Dallara et al [39]. The following paragraphs discuss the changes that

are applied to this model to assess the climate impact for hydrogen aircraft. The most prominent changes come from the elimination of carbon dioxide, soot, and sulfur oxide emissions. The former two eliminations are caused by the lack of carbon atoms in the fuel, while the latter emissions are eradicated, because hydrogen can be produced free of sulfur [43].

### Nitrogen oxides

Nitrogen oxide emissions are still produced in the combustion of hydrogen due to the presence of nitrogen in the air and the relatively high temperatures in the combustion chamber. Nevertheless, hydrogen features wider flammability limits and higher flame speeds than kerosene, allowing a decrease in flame temperature and a reduction in residence time, both curtailing the formation of  $\text{NO}_x$  [25]. It is estimated that these aspects can reduce the  $\text{NO}_x$  emissions by 50–80% [9, 43] through, for example, lean direct injection or micro-mixing technologies [10, 20, 26]. To evaluate the hydrogen-variant aircraft in this study, the emissions per unit of energy are assumed to reduce by 65%, while the interval boundaries are studied in Sect. 5.2.

Although the  $\text{NO}_x$  emissions are reduced, several radiative forcing effects remain. The current model captures three consequences due to  $\text{NO}_x$ : first, short-lived ozone ( $\text{O}_{3\text{S}}$ ) is created, leading to a warming effect. Second, in the long term, methane ( $\text{CH}_4$ ) and long-lived ozone ( $\text{O}_{3\text{L}}$ ) are depleted, causing a cooling effect. The influence of  $\text{NO}_x$  emissions on the mean surface temperature change  $\Delta T$  is assessed using the same model for both kerosene and hydrogen aircraft [35]. Although a reduction in stratospheric water vapor is expected due to  $\text{NO}_x$  emissions [24], this is not considered in the current study.

### Water

The water vapor emissions in the case of hydrogen are significantly higher. The emission index of water vapor can be derived from the chemical reaction in Eq. (10) and amounts to 8.93 kg per kg of hydrogen. This is approximately seven times as high as for kerosene ( $\text{EI}_{\text{H}_2\text{O}} = 1.26\text{kg/kg}$ ). Computing the water vapor per unit of energy yields  $7.44 \times 10^{-2} \text{ kg/MJ}$  and  $2.93 \times 10^{-2} \text{ kg/MJ}$  for hydrogen and kerosene, respectively, a difference of approximately 61%.

The radiative forcing per unit of emitted water mass is assumed to be equal for both aircraft types, namely  $7.43 \times 10^{-15} \text{ W}/(\text{m}^2\text{kg})$ . Hence, the relative contribution of water vapor to the total climate impact is expected to increase when shifting from kerosene to hydrogen. In the model, water emissions are treated as a short-lived gas in the atmosphere, although the lifetime varies with altitude [43].

## Contrails

The increased water vapor content also performs an important role in the formation of contrails behind hydrogen aircraft. A higher water vapor emission index tends to increase the probability of contrail formation [27]. Nevertheless, due to the lack of aerosol emissions, such as soot, the contrail properties are expected to change. These two effects are treated separately in the current model implementation.

Contrails are formed because the exhaust gases from the turbofan engines are hot and humid compared to the atmospheric conditions in which aircraft typically operate, i.e., at altitudes in the upper troposphere or lower stratosphere, with cold and dry air. Under certain atmospheric conditions, ice crystals can form around aerosols which act as nuclei. These conditions are that the ambient temperature is lower than the threshold of 235 K (− 38 °C) and that the Schmidt–Appleman criterion is satisfied [38]. This criterion verifies whether the exhaust gases during the mixing process with ambient air reach saturation with respect to liquid water. This mixing process for a turbofan engine can be modeled as a linear relationship between the water vapor partial pressure  $p^{\text{H}_2\text{O}}$  and the temperature  $T$  of the mixing gas

$$\begin{aligned} p^{\text{H}_2\text{O}} &= p_{\text{amb}}^{\text{H}_2\text{O}} + G \cdot (T - T_{\text{amb}}) \\ &= p_{\text{amb}}^{\text{H}_2\text{O}} + p_{\text{amb}} \cdot c_p \cdot \frac{M_{\text{air}}}{M_{\text{H}_2\text{O}}} \\ &\quad \cdot \frac{\text{EI}_{\text{H}_2\text{O}}}{(1 - \eta_{\text{ov}}) \text{LHV}} \cdot (T - T_{\text{amb}}), \end{aligned} \quad (18)$$

where the slope  $G$  is dependent on the emission index of water, the engine's overall efficiency, and the lower heating value of the fuel. A higher slope results in a larger contrail formation probability, because saturation with respect to liquid water is more likely to occur. In the case of hydrogen fuel, the slope increases due to more water vapor emissions, and it decreases because of the higher calorific value. Furthermore, the exhaust gas composition influences the efficiency, although this effect is lower in magnitude.

Due to a lack of soot emissions in the case of hydrogen combustion, also the contrail properties change. A smaller amount of ice crystals develops initially, although they are larger in size [8, 27, 43]. These aspects in turn reduce the optical depth of the contrails and decrease their lifetime, which lowers the resulting radiative forcing. Based on the literature [8], a 70% reduction in radiative forcing due to contrails is assumed in this study compared to kerosene aircraft, corresponding to a reduction of 90% in initial ice particle number. For the regular, kerosene-based climate model, a radiative forcing of  $1.82 \times 10^{-12} \text{W}/(\text{m}^2 \text{km})$  is assumed for contrails [24].

## 2.2.8 Cash operating cost

Discipline 7 in Fig. 1 assesses the financial operating cost of the aircraft design. Although the operating cost of a hydrogen aircraft are still uncertain, it is important to put the potential climate impact saving into perspective. In the current study, the financial objective function consists of the cash operating cost which includes costs related to flight and maintenance and which are computed according to the cost models introduced by Roskam [37]. Other categories, such as depreciation, fees, and financing costs, are excluded from this analysis to further limit uncertainty. All costs are expressed in US dollars (USD). In the following paragraphs, the flight and maintenance costs are elaborated.

### Flight costs

The costs related to executing missions are divided into three categories: fuel and oil, crew, and insurance. The fuel costs are derived directly from the fuel consumption during the selected mission. For the kerosene aircraft, the fuel price is assumed to be 2.71 USD/US gallon. The cost of sustainable liquid hydrogen is taken to be 4.40 USD/kg (2030 price level) [17], which translates into 1.18 USD/US gallon, corresponding to a decrease of 56% in cost per unit of volume. However, when considering the price per unit of energy, hydrogen is 54% more expensive.

It is recognized that especially this category bears a lot of uncertainty, since fuel prices can be volatile. Some aspects that will perform an important role are the local availability of hydrogen and the means of transport to the airport, while the kerosene price may also vary due to future tax schemes, among other influences. Therefore, the sensitivity of the results to these assumptions is evaluated in Sect. 5.3. The cost of oil is set to 60 USD/US gallon with a density of 7.4 lb/US gallon (887 kg/m<sup>3</sup>). The total oil mass is linearly related to the number of engines and the block time ( $t_{\text{bl}}$ ) [37].

The crew costs are equal for both aircraft types and scale linearly with the block time and therefore inversely with the block speed ( $v_{\text{bl}}$ ). Lower cruise speeds result in longer flight times for a given trip, increasing the cost of cockpit and cabin crews. The following annual salaries are assumed: 277,000 USD for the captain,<sup>1</sup> 188,000 USD for the first officer and 43,160 USD for each cabin crew member<sup>2</sup> [35]. All crew members are expected to fly 1000 h annually.

An annual insurance cost of 0.56% of the market price is assumed, where the latter is calculated according to the

<sup>1</sup> URL <https://epicflightacademy.com/airline-pilot-salary/> retrieved on 24/11/2020.

<sup>2</sup> URL <https://www.indeed.com/cmp/American-Airlines/salaries/Flight-Attendant> retrieved on 24/11/2020.

relation derived in Reference [35]. Since the market price of future hydrogen aircraft is unknown at the time of writing, it is considered to be equal to the price of a kerosene aircraft. Although this may lead to an underestimation of the insurance costs, this category often performs a minor role in the overall cost picture compared to, for example, fuel and crew costs.

### Maintenance

In the calculation of the maintenance expenses, no distinction is made between the two aircraft types. The costs are split up into the expenses associated with the airframe and the expenses required to maintain the engines, both requiring labor hours and materials. For either category, the labor costs of a technician ( $r_{lab}$ ) are estimated to be 33 USD per hour.<sup>3</sup> The total maintenance hours are related to the airframe mass and engine take-off thrust for the airframe and engines, respectively, according to the relations provided by Roskam.

The cost of spare materials is also calculated according to the methods prescribed by Roskam, assuming 5000 flight hours between engine repairs and a spare part price factor of 1.0 compared to the original material. Furthermore, a cost for the maintenance burden is included [37], which accounts for any overhead costs related to maintenance activities.

The choice of maintenance cost model can also influence the cost-optimal design choices. This is caused by different sensitivities with respect to engine mass, bypass ratio, and overall pressure ratio, among other variables. This causes the relative importance of the different cost contributions to vary between models. The impact of the choice of maintenance cost estimation model is therefore further discussed in Sect. 5.3.

### 2.3 Future fleet scenario

Since the climate impact is assessed over a period of 100 years, considering both long- and short-lived effects, a hypothetical, multiyear fleet scenario is defined. This scenario considers the introduction of a new medium-range, narrow-body aircraft in the year 2020. The top-level requirements for this aircraft are summarized in Table 4. These requirements and specifications are similar to those of the Airbus A320-200 [2, 19].<sup>4</sup> Although the aircraft is designed for the specified harmonic range and payload combination, the performance is evaluated for a mission of 1852 km (1000 nmi) with a payload of 13 metrics tons, corresponding to 130

**Table 4** Top-level aircraft requirements employed for the aircraft design [2, 19]

Requirement [Unit]	Value
Maximum structural payload [metric tons]	18.2
Harmonic range [km (nmi)]	3200 (1730)
Ferry range [km (nmi)]	6750 (3645)
Approach speed [m/s (kts)]	70.0 (136)
Take-off length (ISA conditions) [m (ft)]	2100 (6890)

passengers. This mission represents a frequently operated payload-range combination for the studied aircraft category [16].

The production of the aircraft model starts in 2020 and continues until the year 2050. Each aircraft has a lifetime of 35 years, leading to a reduction in the fleet size after the year 2055 and a complete fleet retirement in 2085. Between 2050 and 2055, the fleet size is constant and at its maximum. In this period, an annual, fleet-wide productivity of  $3.95 \times 10^{12}$  revenue passenger kilometer (RPK) is assumed based on past flight operations [44] and future projections [1, 6]. This productivity determines the total number of aircraft required in that 5-year period according to the following relation [35]:

$$N_{AC, 2050} = \frac{\text{Productivity}_{2050}[\text{RPK}]}{\text{Capacity} [\text{passengers} / \text{flight}] \cdot r_{bl}[\text{km}]} \cdot \frac{t_{bl}[\text{h}]}{U_{ann}[\text{h}]} \\ = \frac{3.95 \cdot 10^{12}}{130 \cdot 1852} \cdot \frac{t_{bl}}{3700}, \quad (19)$$

where it is assumed that the annual utilization of a medium-range aircraft is approximately 3900 h per year. This relation simulates that the number of required aircraft to meet the productivity constraint is linearly related with the block time and therefore inversely related with the cruise speed of the aircraft.

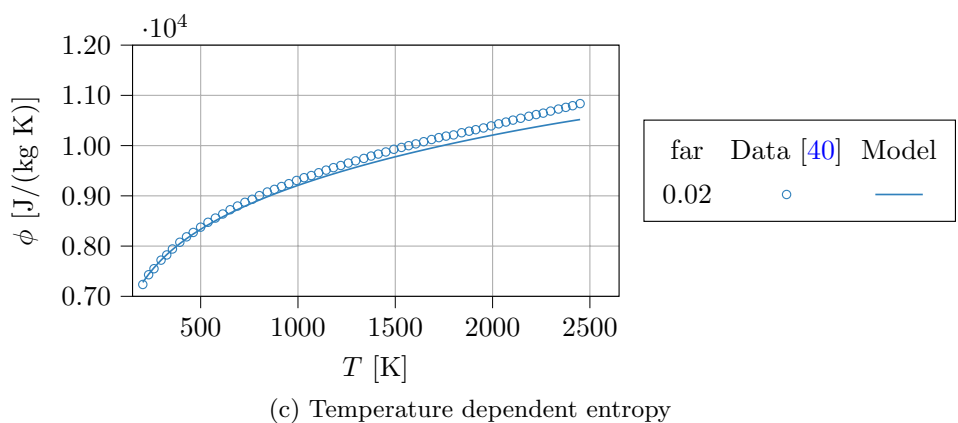
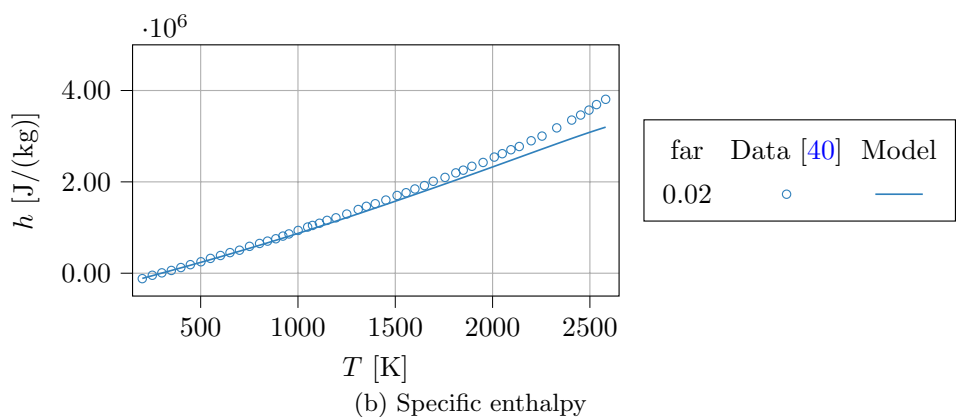
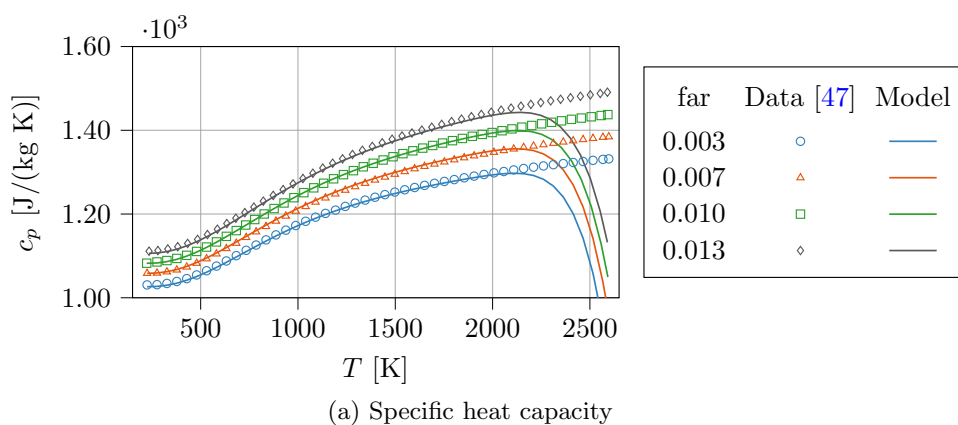
## 3 Verification

The verification of the design and analysis framework introduced in Sect. 2.2 has been discussed in previous research [35]. The current section aims to verify whether this simplified model introduced in Sect. 2.2.5 accurately estimates the gas properties of hydrogen combustion products. Therefore, the model is compared to data provided by Verstraete [47] and Sethi [40]. Figure 6a–c shows the comparison for three key parameters from Eq. (9). It appears that the model agrees well with the data up to temperatures of around 2000 K. Beyond this temperature, chemical dissociation takes place, which is not captured by the current model. Nevertheless, since turbine temperatures are limited to 2000 K, this does not pose an issue. Additionally, the enthalpy and entropy

<sup>3</sup> URL <https://www.indeed.com/career/aircraft-mechanic/salaries> retrieved on 30/08/2022.

<sup>4</sup> URL <https://booksite.elsevier.com/9780340741528/appendices/data-a/table-1/table.htm> retrieved on 25/08/2022.

**Fig. 6** Verification of gas model parameters as functions of temperature for hydrogen combustion products (far = fuel-to-air ratio)



data in Fig. 6b and c, respectively, consider a non-zero water-to-air ratio which explains a minor underestimation (2-5%) of the model in the graphs.

## 4 Results

With the methods introduced above, we initiate design optimizations for different objectives. The three objectives of interest in this study are the climate impact, measured by  $ATR_{100}$ , the cash operating cost (COC), and the energy

consumption ( $E_{fuel}$ ), which relates directly to the fuel consumption. This chapter presents the optimized designs in Sect. 4.1 and compares the performance of the kerosene and hydrogen concepts in Sect. 4.2.

### 4.1 Optimized aircraft solutions

This section presents the optimized aircraft solutions and discusses the rationale behind the design decisions. Table 5 introduces the design vectors that lead to the minimization of the respective objectives for the kerosene

**Table 5** Optimized design variables for the three design objectives

Variable [Unit]	Kerosene			Liquid hydrogen		
	ATR	COC	Energy	ATR	COC	Energy
$A$ [-]	11.2	7.72	11.5	10.3	10.3	11.3
$W/S$ [kN/m <sup>2</sup> ]	5.53	5.30	5.95	5.42	5.15	5.50
BPR [-]	10.9	8.43	10.0	10.0	8.83	9.77
$\Pi_{fan}$ [-]	1.39	1.69	1.55	1.53	1.75	1.70
$\Pi_{ipc}$ [-]	1.48	1.58	1.56	1.56	1.67	1.50
$\Pi_{hpc}$ [-]	20.4	22.3	24.1	21.7	20.5	22.3
TET [ $10^3$ K]	1.38	1.52	1.43	1.46	1.47	1.47
$h_{cr}$ [km]	6.01	9.74	10.4	6.02	10.9	10.8
$M_{cr}$ [-]	0.508	0.802	0.726	0.575	0.760	0.720

**Table 6** Optimized objective values and the relative change with respect to minima obtained for the kerosene aircraft

Parameter [Unit]	ATR*	COC*	Energy*
ATR [mK]	8.3* (-)	23.2 (+180%)	21.6 (+161%)
COC [ $10^{12}$ USD]	9.7 (+17%)	8.3* (-)	8.6 (+3%)
Energy [ $10^{12}$ MJ]	4.54 (+8%)	4.69 (+11%)	4.22* (-)

**Table 7** Optimized objective values and the relative change with respect to minima obtained for the hydrogen aircraft

Parameter [Unit]	ATR*	COC*	Energy*
ATR [mK]	0.2* (-)	6.3 (+2494%)	6.2 (+2446%)
COC [ $10^{12}$ USD]	11.5 (+9%)	10.6* (-)	10.6 (0%)
Energy [ $10^{12}$ MJ]	4.83 (+9%)	4.53 (+3%)	4.41* (-)

and hydrogen aircraft. For clarity, the optimal solutions designs are treated first per fuel type, after which a comparison is provided in Sect. 4.2.

#### 4.1.1 Kerosene

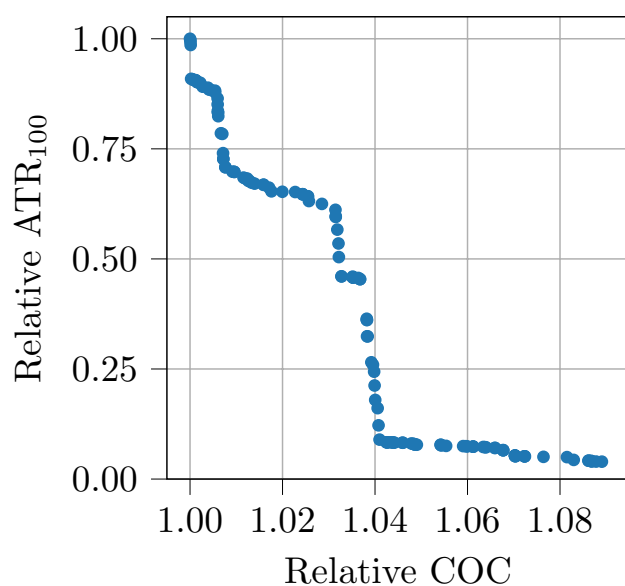
The optimization of kerosene aircraft for cost, fuel burn, and climate objectives was the focus of previous research [35], and therefore, the design solutions are not discussed elaborately in the current section. The objective function values and relative differences are summarized in Table 6. On the diagonal of the table, the minimum values are shown for each objective function. Off-diagonal entries show the relative change in each performance metric listed in the left column when the aircraft is optimized for the performance metric in the header row, marked with an asterisk.

Table 5 presents the optimal design vector for the cost-optimal aircraft. It can be observed that the cruise Mach number is higher than for the other objectives, reducing the mission block time and, as a consequence, the crew and maintenance costs. This Mach number leads to the maximum lift coefficient of 2.49. The engine features an OPR of approximately 59.9, which is close to the maximum allowed value of 60 and higher than for climate-optimal solution (42.0). The bypass ratio of 8.43, which is lower than for the energy- and climate-optimal aircraft, provides a balance

between fuel consumption and engine mass, which drives the related maintenance costs. Although the cost-optimal kerosene aircraft design is similar to current medium-range aircraft, its bypass ratio and aspect ratio are slightly lower than current trends. It is expected that this is partially caused by the selected model for maintenance cost. This aspect is further discussed in Sect. 5.3.

The kerosene, cost-optimal aircraft has the largest climate impact of all cases considered in this paper. The main contributors to the climate impact of this aircraft are persistent contrail formation, carbon dioxide emissions, and nitrogen oxide emissions at altitude. Compared to the energy-optimal, kerosene aircraft, the CO<sub>2</sub> emissions are higher due to the higher fuel consumption. When the climate objective is selected for the kerosene aircraft optimization, the aircraft flies lower and slower and features a lower engine OPR. These changes reduce the ATR<sub>100</sub> by approximately 64%. The lower cruise altitude prevents the formation of persistent contrails and reduces the radiative forcing due to ozone creation as a consequence of NO<sub>x</sub> emissions. Additionally, the lower engine OPR reduces the emissions index of NO<sub>x</sub>. However, these changes also lead to a reduction in turbofan efficiency and non-optimal fuel consumption. This makes the CO<sub>2</sub> emissions the largest contributor to the climate impact of the climate-optimal, kerosene aircraft. For this reason, it is expected that liquid hydrogen can further reduce the climate impact.





**Fig. 7** Pareto front of cost- and climate-optimal hydrogen solutions, relative to the cost-optimal design

#### 4.1.2 Liquid hydrogen

In Table 7, the optimization results for the three different objectives are shown. This shows that the absolute minimal ATR value for a fleet of medium-range, liquid-hydrogen aircraft is estimated to be approximately 0.2 mK. However, if the objective function changes to minimum energy consumption or cash operating cost, the average temperature response is an order of magnitude higher. The trade-off between the cost- and climate-optimal designs is presented graphically in Fig. 7.

The climate-optimal, hydrogen aircraft is characterized by its low cruise altitude ( $h_{cr} = 6.0$  km) and Mach number ( $M_{cr} = 0.58$ ). First, this low-altitude operation eliminates contrail formation, since the criteria are not met according to the ISA model. Contrails have the largest contribution to the climate impact of hydrogen aircraft, and their elimination thus largely reduces the average temperature response. Second, the impact of  $\text{NO}_x$  emissions is also minimized at this altitude, even leading to potentially negative radiative forcing in the long term.

These two effects can be observed in Fig. 8 where the variation in radiative forcing and  $\Delta T$  over the considered period are shown for the three climate agents. It can be deduced that the elimination of the persistent contrails in the ATR-optimal case significantly reduces the temperature response. While the long-term effects of  $\text{NO}_x$ , namely methane and ozone depletion, cause the radiative forcing to become negative for all three objectives, it only causes a negative temperature response for the climate-optimal design due to its low-altitude operation. These two effects

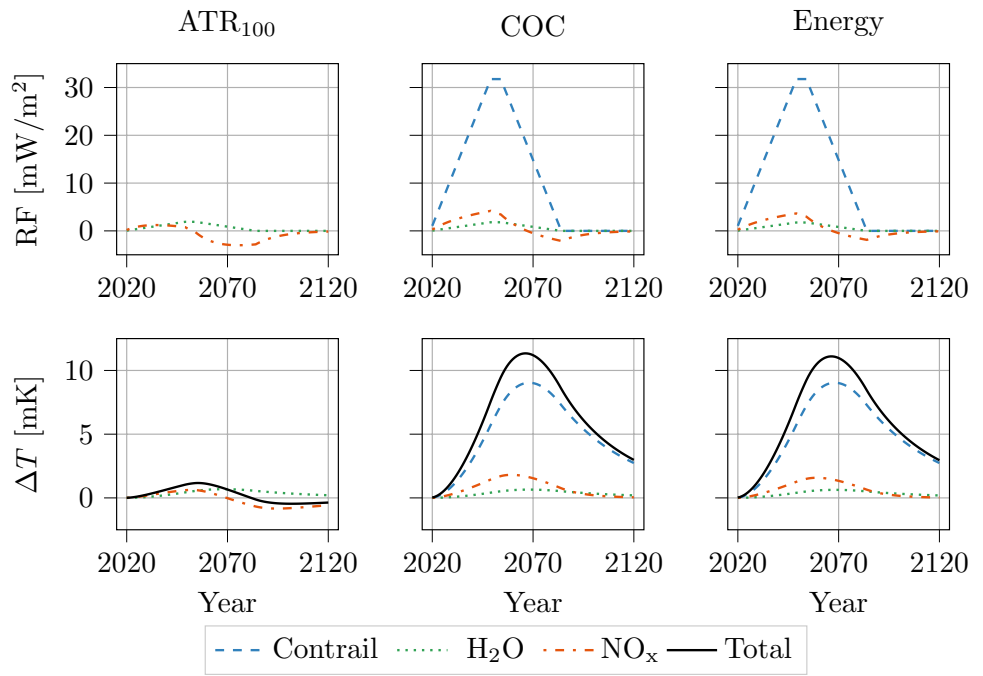
lead to a difference of an order magnitude in ATR between the climate-optimal solution and the other two designs. The influence of water vapor as a greenhouse gas is comparable for all three hydrogen aircraft, although the contribution to  $\text{ATR}_{100}$  is larger than for kerosene aircraft. The residence time of water vapor in the atmosphere increases with altitude, which is not considered in the current climate model. Therefore, it is expected that the climate impact of  $\text{H}_2\text{O}$  will be higher for the aircraft operating at higher altitudes, such as the energy- and cost-optimal designs, compared to the one operating at approximately 6.0 km of altitude.

The climate-optimal aircraft features an unswept wing with an aspect ratio of 10.3 and the maximum achievable  $C_{L,max}$  of 2.80, which is facilitated by the Mach number of 0.58. The wing loading is not set to the maximum value limited by the approach speed, but rather close to the  $W/S$  value which minimizes the  $T_{TO}/W$  ratio. This occurs at the intersection of the OEI climb and take-off constraints. A bypass ratio of 10.0 is selected with an OPR of 51.8. This combination minimizes the combined impact of  $\text{NO}_x$  and water vapor emissions. In the selection of the engine variables, two aspects have to be considered: first, the fuel consumption has to be reduced to lower the total emissions, in particular those of water vapor. Second, a high OPR will lead to an increased emission index of  $\text{NO}_x$ . These two considerations have to be balanced. Also, since the  $\text{NO}_x$  emissions at this altitude lead to a cooling effect, the optimizer does not try to minimize fuel burn but makes use of slightly higher absolute  $\text{NO}_x$  emissions to increase this radiative cooling effect. Nevertheless, a realistic alternative would be to focus on fuel burn reduction while operating at this altitude.

The cost-optimal hydrogen aircraft features the highest cruise Mach number (0.76) and cruise altitude (10.9 km) of the three hydrogen aircraft. The higher cruise velocity, compared to the climate-optimized solution, is crucial to lowering the time-related operating cost. The altitude is increased simultaneously to achieve a near-optimal lift-to-drag ratio to minimize energy consumption. The wing features a quarter-chord sweep angle of 23 degrees as a consequence of the selected cruise Mach number. This limits the achievable  $C_{L,max}$  to 2.58 in landing configuration and, as a result, the wing loading. The wing loading is not set to the maximum value allowed for the approach, allowing for a lower  $T/W$  at take-off. The aspect ratio of 10.9 does not reach the upper limit of 12, although the span limit is almost reached. The optimizer selects a bypass ratio of 10.9 in combination with an OPR of 60, which is the upper limit.

The energy-optimal aircraft features similar design characteristics as the cost-optimal aircraft, since the operating cost of the hydrogen aircraft is largely driven by the fuel cost. The energy-optimal aircraft cruises at an altitude and Mach number in between the climate- and cost-optimal solutions. A Mach number of 0.72 is selected, requiring less

**Fig. 8** Contribution of individual climate agents to radiative forcing (RF) and surface temperature change ( $\Delta T$ ) for the optimized hydrogen aircraft. The title above each column indicates the optimization objective that has been used to design the aircraft



sweep than the cost-optimal aircraft and allowing a higher maximum lift coefficient. This allows for a higher wing loading, compared to the cost-optimal case, and therefore a higher aspect ratio. The wing loading is set to the maximum value allowed to facilitate an approach speed of 70 m/s. With an aspect ratio of 11.3, the wing planform reaches the span limit of 36 m. Also, the buffet constraint is active. Without considering the engine maintenance costs, the optimizer is free to further increase the engine bypass ratio with an OPR value of 57.

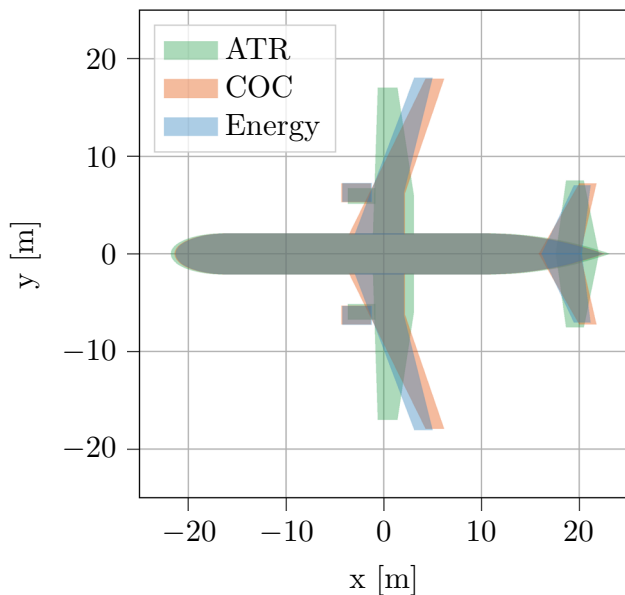


**Fig. 9** Top view of the optimized hydrogen aircraft, where  $x=0$  lies on the quarter-chord point of the MAC

Figure 9 presents the overlapping top views of the three different hydrogen aircraft. The geometries of the cost- and energy-optimal concepts are rather similar, although the energy-optimal aircraft has a slightly more slender wing and a lower sweep angle. A clear distinction with the climate-optimal aircraft can be observed. First, the quarter-chord wing sweep is zero due to the lower cruise Mach number. Second, the fuselage of the climate-optimal aircraft is slightly longer. The climate-optimal aircraft features an engine with lower overall efficiency, due to its operating conditions, resulting in a lower range parameter ( $p = \eta_{ov} \cdot L/D$ ). This leads to deteriorating fuel consumption and an increase in the fuel mass required to achieve the ferry range. Since the fuel tank is sized for this maximum fuel capacity, the fuselage is longer, in turn leading to more friction drag and worsening the range parameter further. It is expected that in this case, relaxing the ferry requirement would lead to

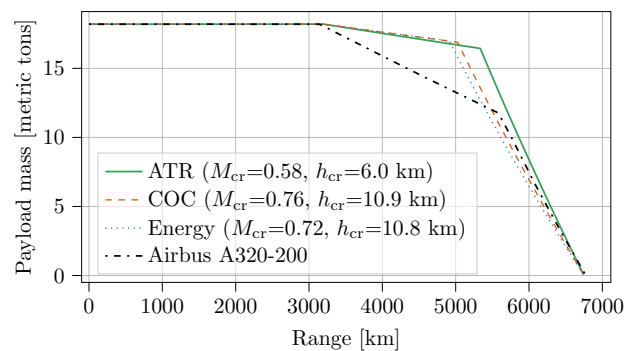


**Fig. 10** Payload-range diagram of the hydrogen aircraft optimized for three different objectives and the diagram of the Airbus A320-200 [2]

improved flight performance and climate impact, while still being able to serve a large part of the payload-range envelope of the Airbus A320-200, for example.

Figure 10 presents the payload-range diagrams for the optimized hydrogen aircraft and compares them to the diagram of the Airbus A320-200. It can be observed that all three hydrogen aircraft have a wider payload-range capability than the Airbus A320-200, caused by the harmonic and ferry range requirements and the higher calorific value of hydrogen. The latter allows achieving a larger range increase with a lower exchange of payload for fuel mass, compared to kerosene. The payload-range envelop of the climate-optimal, hydrogen aircraft also reveals its marginally worse cruise performance compared to the two other designs because of the lower range parameter.

## 4.2 Comparison between kerosene and liquid hydrogen aircraft

Whereas the previous section focused on the optimized results and the aircraft design rationale behind them, the current section aims to investigate how the liquid hydrogen alternative compares to the kerosene solution in terms of cost, climate impact, and other performance indicators. These performance indicators are presented in Table 8.

By examining the data provided in Tables 6 and 7, it can be concluded that with respect to the cost-optimal, kerosene aircraft, the cost-optimal hydrogen aircraft can achieve a 73% decrease in average temperature response for the period under consideration, at a 28% cash operating cost increase (assuming a liquid hydrogen price of 4.40 USD/kg). An even larger climate impact reduction can be achieved by optimizing minimum climate impact, yielding a 99% reduction in  $ATR_{100}$  with an approximate 39% increase in cost. The trade-off between climate impact and cash operating cost for each aircraft type, and between them, is graphically represented by the Pareto fronts in Fig. 11, where also the influence of varying fuel prices is shown. The reason for this immense climate saving potential stems from the eradication of  $CO_2$  emissions and reduction in  $NO_x$  emissions, as well as the different contrail properties. The cost increase follows mainly from the liquid hydrogen price. On the other hand, the ATR-optimized hydrogen aircraft does consume 5% more energy than the energy-optimized hydrogen aircraft and 17% more energy than the energy-optimized kerosene aircraft. Since the climate-optimal, hydrogen aircraft suffers from this energy penalty, it also has the largest tank of all three objectives and therefore the longest fuselage.

Table 8 presents the performance indicators and geometric parameters for all optimized aircraft. It can be observed that the hydrogen aircraft feature, on average, a 5% lower maximum take-off mass and a 9% increase in operating empty mass compared to the kerosene counterparts. This is

primarily caused by the addition of the large fuel tank and the resulting stretch of the fuselage ( $l_{fus}$  in Table 8). The wing areas are rather similar for all solutions. While the hydrogen aircraft have a lower MTOM, the wing loading is also lower because of the higher maximum landing mass. Therefore, the net difference in wing area is quite small compared to the kerosene aircraft.

From a flight performance perspective, the climate- and energy-optimal hydrogen aircraft are characterized by a lower lift-to-drag ratio in cruise than their kerosene counterparts. This is largely caused by increased friction drag due to the longer fuselage and larger horizontal tail area. For the energy-optimal aircraft, the wetted area of the fuselage with a hydrogen tank is approximately 18% higher than the wetted area of the regular fuselage. On the other hand, the cost-optimal, kerosene aircraft features a lower lift-to-drag than its hydrogen alternative (16.7 versus 17.9). The reason for this is that reducing the fuel cost is more important for the hydrogen aircraft than for the kerosene aircraft, for which the time-bound cost is relatively more important. Therefore, the design of the cost-optimal hydrogen aircraft resembles its energy-optimized variant more closely than the kerosene aircraft, resulting in a higher aerodynamic efficiency.

The engine performance of the hydrogen aircraft sees a 62–66% lower thrust specific fuel consumption due to the higher calorific value of hydrogen. The energy consumption of the energy-optimal, hydrogen aircraft is 4% higher than for the kerosene alternatives. For the cost-optimal aircraft, this trend is again different due to the different relative importance of fuel efficiency.

Finally, Table 8 also provides an estimate of the block time  $t_{bl}$  of the selected mission, as well as the total number of aircraft  $N_{ac,max}$  to be produced. These numbers vary between the objectives, with slower flying designs resulting in higher block times and more aircraft to meet the required productivity level.

## 5 Sensitivities and uncertainties

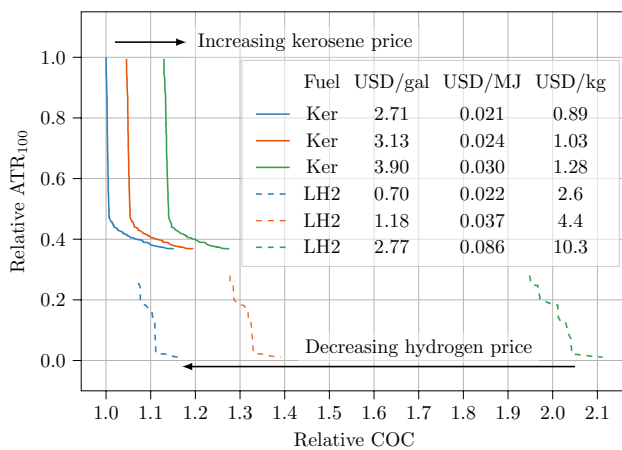
The hypothetical future aircraft designs and scenario discussed in this paper rely on assumptions that have an influence on the objective functions and possibly also the obtained design vector. The aim of this section is to quantify the effect of assumptions related to hydrogen technology, climate modeling, and cost estimation, on the three objective functions considered in the previous section.

### 5.1 Hydrogen technology uncertainty

The first uncertainty is introduced in the conceptual design process of liquid hydrogen aircraft. Although several research projects have looked more closely into the

**Table 8** Performance indicators for optimized aircraft

Parameter [Unit]	Kerosene			Liquid Hydrogen		
	ATR	COC	Energy	ATR	COC	Energy
MTOM [metric tons]	65.1	68.4	68.2	62.1	65.5	64.5
OEM [metric tons]	36.2	39.5	40.3	40.1	43.8	42.8
$S$ [m <sup>2</sup> ]	115	127	112	112	125	115
$b$ [m]	36.0	31.3	36.0	33.9	35.8	36.0
$\Lambda_{0.25}$ [deg]	0.0	27.0	18.9	0.0	23.0	18.0
$\lambda$ [-]	0.460	0.235	0.303	0.460	0.269	0.310
$l_{\text{fus}}$ [m]	37.5	37.5	37.5	44.7	43.7	43.5
$S_{\text{ht}}$ [m <sup>2</sup> ]	31	31	26	45	41	39
$(L/D)_{\text{cr}}$ [-]	19.0	16.7	19.2	16.4	17.9	18.4
$(T/W)_{\text{TO}}$ [-]	0.288	0.315	0.330	0.283	0.295	0.303
$T_{\text{TO}}$ [kN]	184	211	221	172	190	192
$\text{TSFC}_{\text{cr}}$ [ $10^{-5}$ kg/N s]	1.15	1.41	1.28	0.44	0.48	0.46
$\eta_{\text{ov,cr}}$ [%]	32.6	39.9	39.3	34.8	39.3	38.6
$\text{SEC}_{\text{cr}}$ [ $10^{-4}$ MJ/(N s)]	4.93	6.05	5.50	5.22	5.71	5.52
Energy [MJ/(pax km)]	0.82	0.85	0.77	0.90	0.83	0.80
$t_{\text{bl}}$ [h]	4h23m	3h19m	3h34m	4h1m	3h29m	3h36m
$N_{\text{AC,max}}$ [ $10^3$ ]	18.5	14.0	15.0	16.9	14.7	15.2


**Fig. 11** Comparison of kerosene and hydrogen Pareto fronts for varying fuel prices, with respect to the kerosene, cost-optimal design

integration of liquid hydrogen tanks and their mass estimation [20, 21, 31, 49], only several aircraft employing hydrogen as fuel have been realized [12]. We made assumptions with respect to the mass of the tank, which is determined using the gravimetric index, the extra volume allowance, and the geometry of the tank domes.

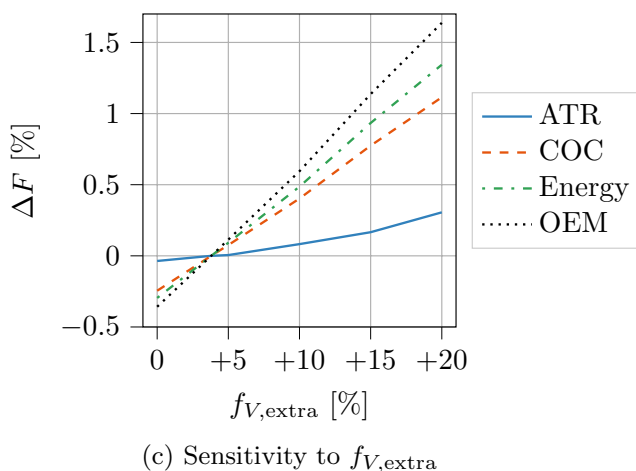
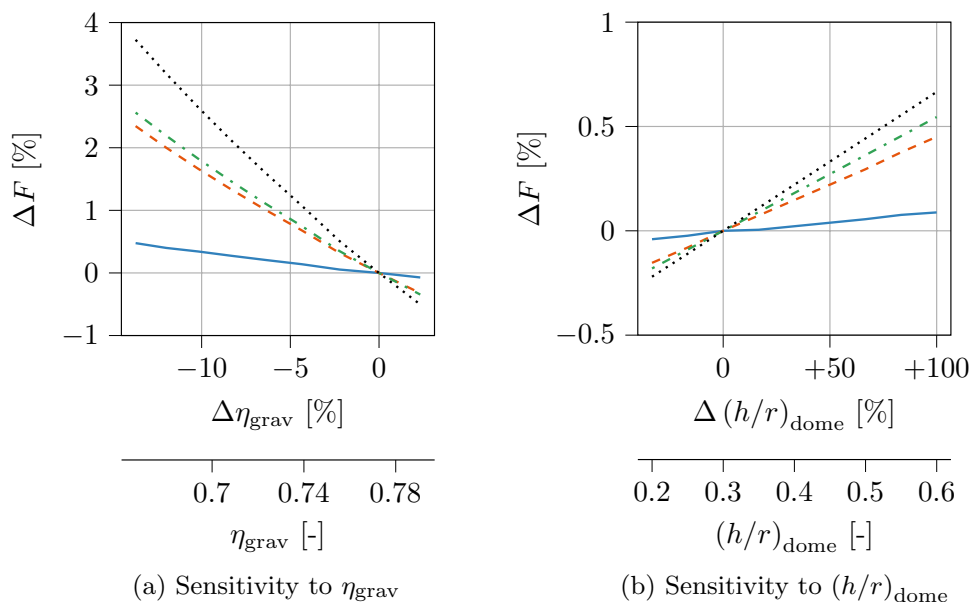
Figure 12a shows the sensitivity of the three objectives with respect to the gravimetric index for the cost-optimized, hydrogen aircraft. The standard value is taken to be 0.773, which is varied between  $-14\%$  (0.661) and  $3\%$  (0.797), associated with varying design choices [31] and technology

scenarios. This value is dependent on the design choices of the tank, such as venting strategy and insulation material choice. From the figure, it can be seen that the gravimetric index has a limited influence on the objective functions, staying within the interval of 3 to  $-1\%$ , for the cost-optimal aircraft. Although the influence on the operating empty mass is marginally larger (up to 4%), this does not appear to propagate significantly through the other design and analyses disciplines.

The sensitivity with respect to the ratio between the dome height and tank radius is presented in Fig. 12b. The evaluated values are selected based on engineering judgment. This sensitivity is smaller than the one with respect to the gravimetric index. Although  $(h/r)_{\text{dome}}$  affects the tank length and hence the fuselage length, the effect seems to be almost negligible, even on the operating empty mass. Possibly, the effect would be higher if the change in dome pressure load due to varying dome radius was considered in the conceptual model.

As mentioned in Sect. 2.2.2, we do not account for gaseous hydrogen inside the tank due to boil-off when computing the internal volume of the tank. This additional volume will result in a longer tank, which elongates the fuselage, increasing the mass and drag of the aircraft. Therefore, we carry out a sensitivity study with the parameter  $f_{V,\text{extra}}$  to quantify the impact of this volume underestimation on the objectives. Figure 12c shows the variation in the objectives as a function of additional fuel tank volume allowance. This analysis shows that when 20% extra volume is considered, the change in objectives appears to be limited to 1.5%. However,

**Fig. 12** Sensitivity of objective functions with respect to hydrogen tank parameters for the cost-optimal aircraft



this sensitivity only considers the effect due to elongation of the tank and fuselage, while an increased volume allowance would also affect the tank gravimetric index. Hence, the actual effect is expected to marginally larger than the sensitivity presented in Fig. 12c.

### 5.2 Climate model uncertainty

The current section aims at quantifying the uncertainty due to climate model assumptions made in Sect. 2.2. The focus lies on the differences between the climate models for the kerosene and hydrogen aircraft, which are the reduction in  $NO_x$  emissions and the reduction in contrail radiative forcing. Although the water vapor emissions change, the effect is not considered here, since the emission index follows from the chemical balance. Furthermore, it is recognized that more uncertainties apply in the linearized temperature

response model. Nevertheless, it is recommended to study and discuss the latter elaborately in separate research.

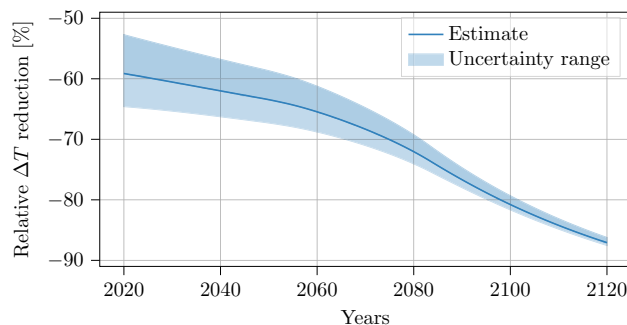


**Fig. 13** Relative surface temperature difference between kerosene and hydrogen, cost-optimal aircraft, including the uncertainty range due to the contrail and  $NO_x$  assumptions made in Sect. 2.2

**Table 9** Optimized design variables for the cost-optimal, kerosene-powered aircraft, considering two different maintenance cost estimation methods

Variable [Unit]	Roskam	AEA
A [-]	7.72	10.0
W/S [kN/m <sup>2</sup> ]	5.30	5.25
BPR [-]	8.43	10.2
$\Pi_{fan}$ [-]	1.69	1.68
$\Pi_{ipc}$ [-]	1.58	1.49
$\Pi_{hpc}$ [-]	22.3	19.9
TET [10 <sup>3</sup> K]	1.52	1.51
$h_{cr}$ [km]	9.74	10.7
$M_{cr}$ [-]	0.802	0.777

Figure 13 shows the relative difference in temperature response between the kerosene and hydrogen, cost-optimal aircraft for the period under consideration. The estimated line corresponds to the model as employed for the optimizations, assuming a 65% reduction NO<sub>x</sub> emissions and a 70% reduction in contrail radiative forcing. The blue band indicates the uncertainty range, considering a interval between 50 and 80% reduction in NO<sub>x</sub> emissions [9] and the 90% confidence interval provided by Burkhardt et al. [8]. It can be observed that the uncertainty reduces in time, because the uncertainties apply mainly to short-lived effects. Additionally, the overall temperature reduction increases with time, because the long-term CO<sub>2</sub> impact is eliminated for the hydrogen aircraft. In summary, the studied uncertainties lead to a variation in ATR reduction between 70 and 75% for the cost-optimal aircraft.

### 5.3 Cost model uncertainty

In this section, we focus on the uncertainties present in the estimation of the operating cost. We consider two aspects, namely the cost model itself, and the assumed fuel prices, in particular for liquid hydrogen.

The cost model selection can influence the relative importance of fuel- and time-related costs. Examples of the latter group are crew and maintenance costs. This relative importance will favor design choices which minimize fuel impact, reduce flight time, and/or reduce maintenance costs. In the selected cost model, the maintenance costs are in particular sensitive to the engine mass, which is greatly influenced by the chosen bypass ratio. For this reason, the cost-optimal bypass ratio of the kerosene aircraft is lower than current technology standards. Implementation of the AEA model [3, 23] leads to a cost-optimal result with a higher bypass ratio and increased wing aspect ratio, as shown in Table 9. However, the optimal OPR is reduced, since the AEA maintenance cost estimation is more sensitive to the overall

pressure ratio. Nevertheless, the observed trends when moving from the cost-optimal to the climate-optimal solution remain similar, except that the cost-optimal solution may be closer to either an energy minimizing or time-bound cost minimizing design points.

Since future operational costs are uncertain for both aircraft types, here the sensitivity of the results with respect to the fuel costs is evaluated. For the hydrogen aircraft, a fuel price of 4.40 USD/kg has been assumed [17] in Sect. 4. During the optimizations, a kerosene price of 2.71 USD/gal is assumed. However, recently the price has been closer to 3.13<sup>5</sup> or has even reached 3.90 USD/gal in May 2022.<sup>6</sup> For kerosene, the cost is varied between 2.71 USD/gal and 3.90 USD/gal. Current price estimates of liquid hydrogen are closer to 10.3 USD/kg. The Pareto front in this case shows a cash operating cost difference of 95–111% between kerosene and hydrogen aircraft. Nevertheless, beyond 2030, the price of hydrogen is expected to decrease further, potentially up to 2.6 USD/kg [9]. Considering these projections, the cost of liquid hydrogen is varied between 2.6 and 10.3 USD/kg in this uncertainty analysis.

Figure 11 presents the effect of varying fuel prices and the trade-off between cost- and climate-optimal designs. The figure shows that the higher kerosene fuel cost and lower hydrogen fuel cost bring the Pareto fronts closer together. Since it is expected kerosene prices will continue to rise in the future [9], possible also because of kerosene taxes, it is clear that the hydrogen and kerosene solution will slowly converge in terms of operating cost.

## 6 Conclusions and recommendations

The objective of this research is to further explore the potential of liquid hydrogen to power future commercial aviation by performing multidisciplinary design optimizations of hydrogen aircraft and comparing the solutions to kerosene designs. First, a medium-range, hydrogen aircraft is optimized for three objectives, being the energy consumption, cash operating cost, and the average temperature response over a period of 100 years. It is found that the energy- and cost-optimal aircraft are similar due to the large contribution of fuel cost. These aircraft have engines with high bypass and pressure ratios and operate at approximately 10.8–10.9 km of altitude and a Mach number of 0.72–0.76. The climate-optimal aircraft significantly reduces ATR<sub>100</sub> by almost an order of magnitude, by flying at an altitude

<sup>5</sup> URL <https://www.iata.org/en/publications/economics/fuel-monitor/> retrieved on 28/09/2022.

<sup>6</sup> URL <https://www.indexmundi.com/commodities/?commodity=jet-fuel&months=120> retrieved on 29/08/2021.

of 6.0 km and Mach number of 0.58, completely eliminating persistent contrail formation and limiting the radiative effects of short-term ozone creation due to  $\text{NO}_x$ .

Second, it can be observed that the hydrogen cost- and climate-optimal aircraft lead to reductions of 73–99% in average temperature response, respectively, compared to the cost-optimal kerosene aircraft. This is caused by the lack of  $\text{CO}_2$  emissions, reduced  $\text{NO}_x$  emissions, and different contrail properties. Nevertheless, the costs are increased by 28–39% because of high hydrogen fuel prices (4.40 USD/kg) and increased energy consumption. The latter is caused by an increase in OEM and a reduction in cruise lift-to-drag ratio, resulting from increased fuselage length due the integration of the liquid hydrogen tank.

Although this research indicates that hydrogen has a large potential to limit the climate impact of aircraft in the studied category, it comes at the expense of increased financial costs. Additionally, the uncertainty in terms of non- $\text{CO}_2$  climate impact and future liquid hydrogen prices has to be recognized. To further improve the performance of the hydrogen aircraft, the following design options can be studied: reducing the maximum fuel capacity by carefully considering future operator requirements, allows a smaller tank size and lower fuselage mass penalty. Furthermore, removing the span constraint and/or applying foldable wing tips could allow for a higher  $L/D$ , reducing the energy consumption.

## Appendix A: Optimization setup and convergence

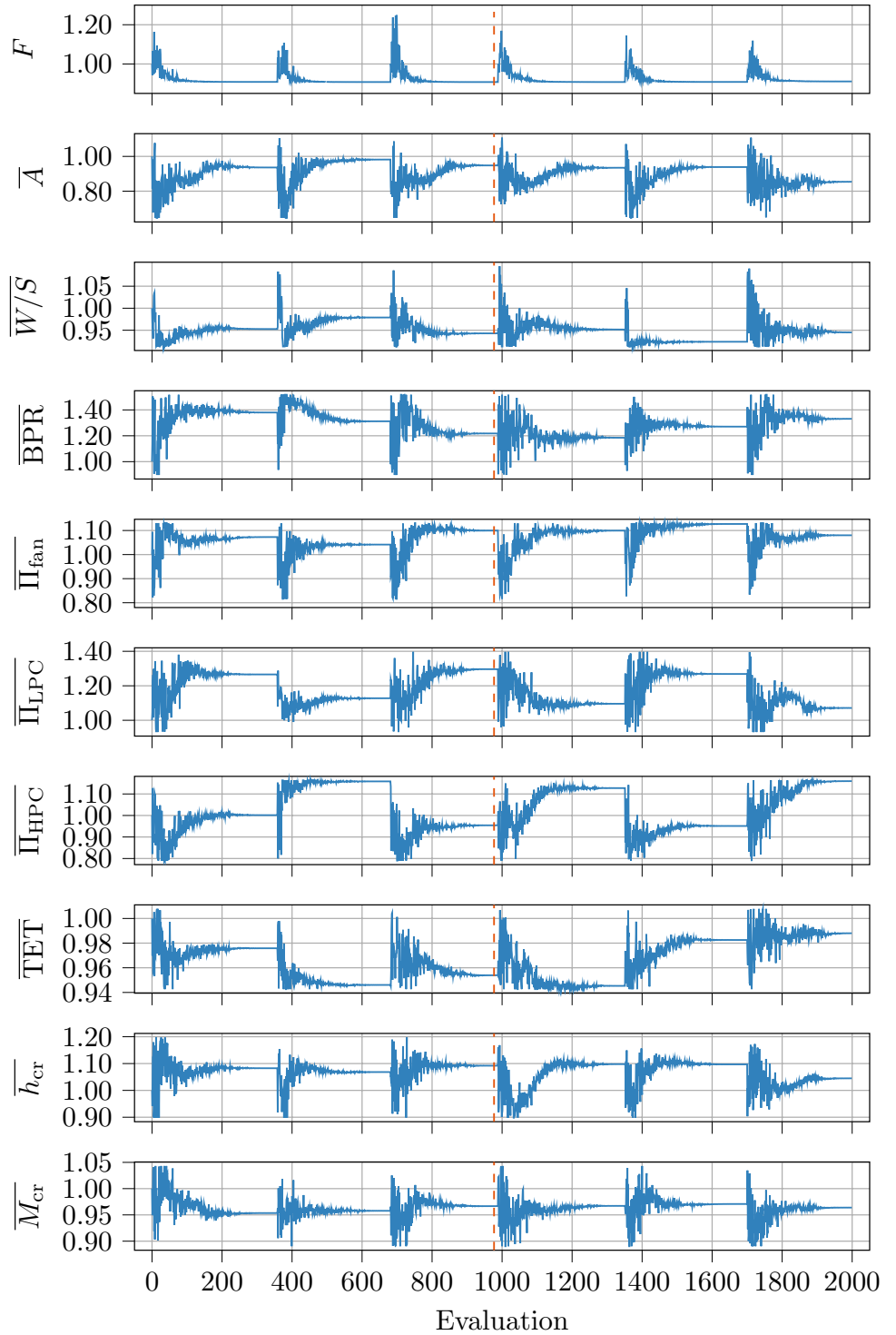
This appendix focuses on the setup of the optimization approach and discusses the convergence of the single- and multi-objective MDO runs. The single-objective optimization consists of two automated steps. First, a design of experiments (DOE) of the nine design variables is performed using Latin Hypercube Sampling (LHS). This DOE is subsequently used to start the optimization with the

Simplex algorithm. We use the software modeFRONTIER<sup>7</sup> to carry out both steps. The implemented Simplex algorithm is the Nelder–Mead approach, where constraints are handled through constraint domination. This algorithm is selected, because it can solve non-linear, constrained problems and because it is more robust than gradient-based methods for the problem under consideration. We apply two termination criteria for the optimization algorithm, being the final termination accuracy (based on the difference of the objective function values in one simplex) of  $1 \times 10^{-5}$  and a maximum number of function evaluations of 2000. If the first termination accuracy is reached before the second criterion, the program automatically restarts at a different point in the design space. This feature helps with avoiding that the optimum found is a local minimum. Figure 14 presents the convergence plots of the single-objective optimization of the hydrogen aircraft for minimal cash operating cost. Figure 15 shows the values of the inequality constraints. These figures also show the automated restarts.

To carry out the multi-objective optimizations (as shown in Figs. 7 and 11), the multi-strategy piOPT algorithm is used. This method considers several optimization strategies and selects the most appropriate one based on the problem characteristics. We use the hypervolume indicator [14] to verify the convergence of the multi-objective optimization. Figure 16a shows the hypervolume convergence for the Pareto front in Fig. 7. Figure 16b shows the difference in hypervolume indicator between a Pareto front evaluated at design evaluation  $i$  and the Pareto front at design evaluation  $i - 100$ . After 6000 evaluations, this difference is smaller than  $1.5 \times 10^{-5}$ , indicating that further potential improvements in the Pareto-optimal set are limited.

<sup>7</sup> URL <https://engineering.esteco.com/modefrontier> accessed on 12/07/2023.

**Fig. 14** Convergence plots of objective function and design variables for cash operating cost minimization of the hydrogen aircraft. The orange, dashed line indicates the optimum. The values are normalized with respect to the first evaluation





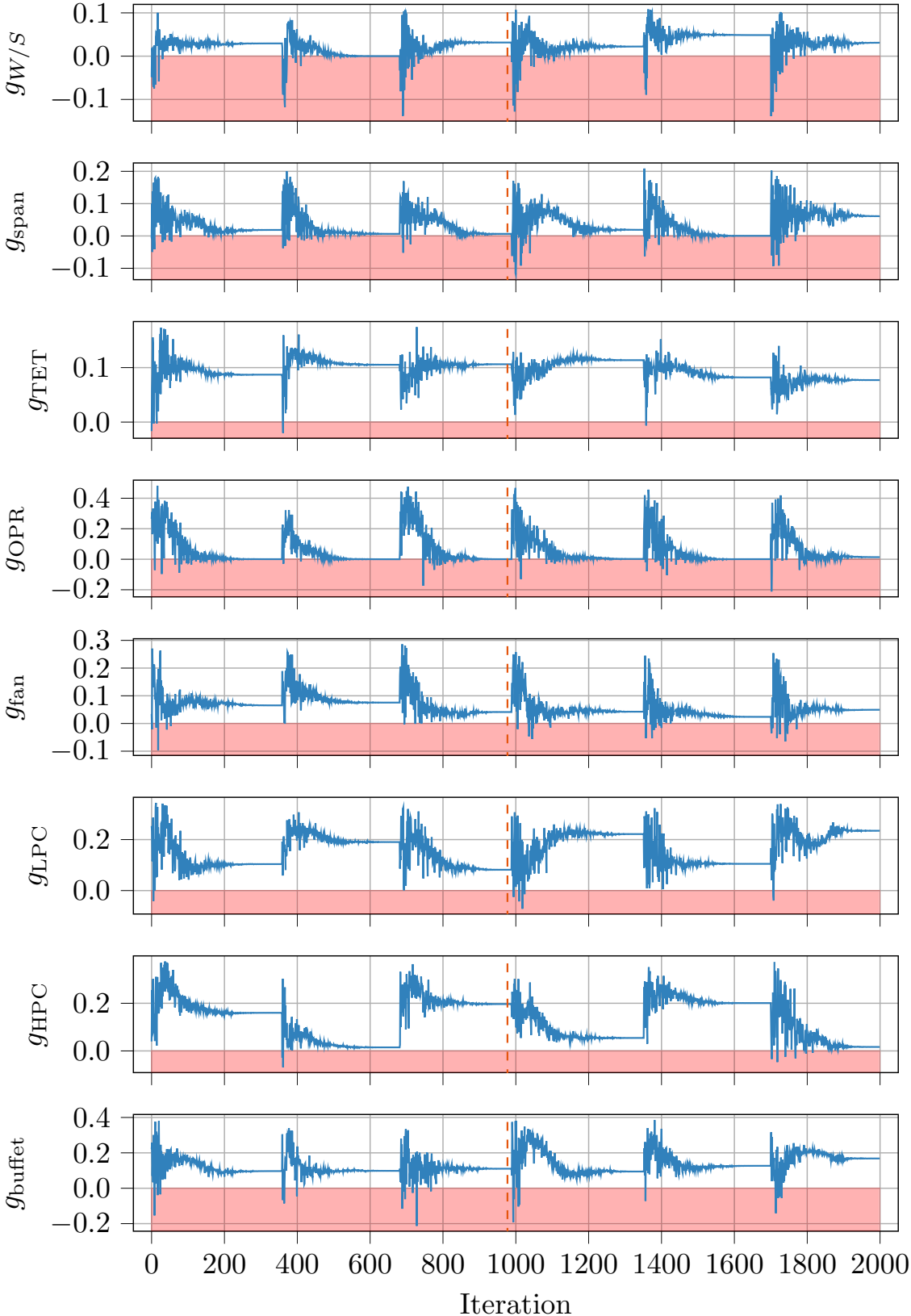
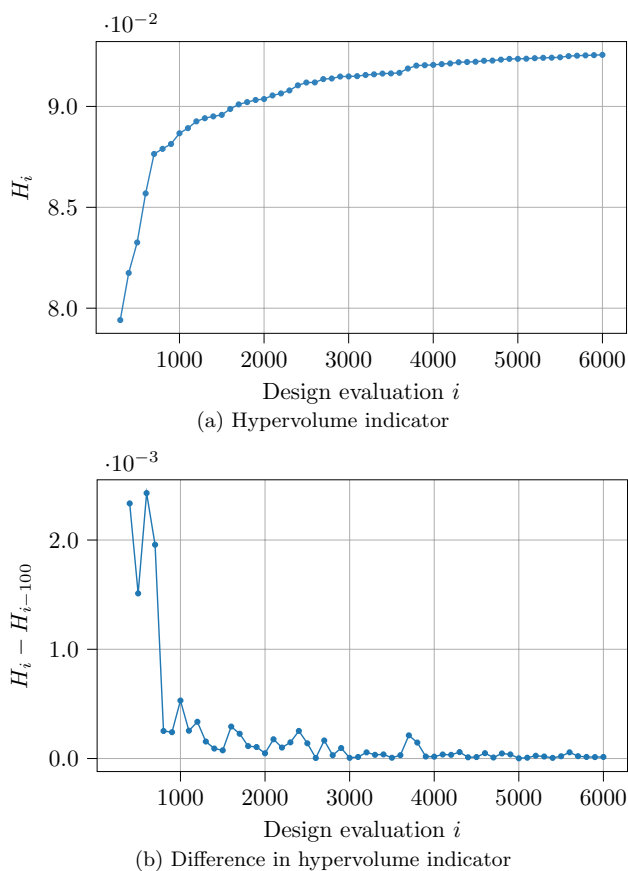


Fig. 15 Convergence plots of constraints for cash operating cost minimization of the hydrogen aircraft. The orange, dashed line indicates the optimum. The red shaded area indicates constraint violation



**Fig. 16** Convergence plot hypervolume indicator  $H$  for the multi-objective optimization of the hydrogen aircraft. The hypervolume indicator is evaluated at each mark, with respect to the point (1.1, 1.1)

**Acknowledgements** This research is sponsored by the European Union's Clean Sky 2 Thematic Topics Program (H2020-EU.3.4.5.10.) under Grant Agreement Nr. 865300.

**Data availability** Not applicable.

## Declarations

**Conflict of interest** The authors have no conflict of interest to declare that are relevant to the content of this article.

**Open Access** This article is licensed under a Creative Commons Attribution 4.0 International License, which permits use, sharing, adaptation, distribution and reproduction in any medium or format, as long as you give appropriate credit to the original author(s) and the source, provide a link to the Creative Commons licence, and indicate if changes were made. The images or other third party material in this article are included in the article's Creative Commons licence, unless indicated otherwise in a credit line to the material. If material is not included in the article's Creative Commons licence and your intended use is not permitted by statutory regulation or exceeds the permitted use, you will need to obtain permission directly from the copyright holder. To view a copy of this licence, visit <http://creativecommons.org/licenses/by/4.0/>.

## References

1. Airbus: Global Market Forecast—Cities, Airports and Aircraft 2019–2038, 5th edn. Airbus S.A.S, Blagnac Cedex (2019)
2. Airbus S.A.S. Customer Services: Airbus a320 Aircraft Characteristics Airport and Maintenance Planning. Tech. rep., Airbus S.A.S. Customer Services (2019)
3. Al-Shamma, O., Ali, R.: A comparative study of cost estimation models used for preliminary aircraft design. *Glob. J. Res. Eng.: B Autom. Eng.* **14**(4) (2014)
4. Antoine, N.E., Kroo, I.M.: Framework for aircraft conceptual design and environmental performance studies. *AIAA J.* **43**(10), 2100–2109 (2005). <https://doi.org/10.2514/1.13017>
5. Boeing Commercial Airplanes: Boeing 737 airplane characteristics and airport planning. Tech. rep, Boeing Commercial Airplanes (2013)
6. Boeing: Commercial Market Outlook 2019-2038. Boeing (2019)
7. Brewer, G.D.: Hydrogen Aircraft Technology. CRC Press (1991)
8. Burkhardt, U., Bock, L., Bier, A.: Mitigating the contrail cirrus climate impact by reducing aircraft soot number emissions. *NPJ Clim. Atmos. Sci.* **1**(1), 37 (2018). <https://doi.org/10.1038/s41612-018-0046-4>
9. Clean Sky 2 JU and Fuel Cells and Hydrogen 2 JU. Hydrogen-powered aviation: a fact-based study of hydrogen technology, economics, and climate impact by 2050. Tech. rep., (2020) <https://doi.org/10.2843/471510>
10. Dahl, G., Suttrop, F.: Engine control and low-nox combustion for hydrogen fuelled aircraft gas turbines. *Int. J. Hydrogen Energy* **23**(8), 695–704 (1998). [https://doi.org/10.1016/S0360-3199\(97\)00115-8](https://doi.org/10.1016/S0360-3199(97)00115-8)
11. Dallara, E.S., Kroo, I.: Aircraft design for reduced climate impact. In: 49th AIAA Aerospace Sciences Meeting including the New Horizons Forum and Aerospace Exposition. American Institute of Aeronautics and Astronautics, Orlando, Florida (2011) <https://doi.org/10.2514/6.2011-265>
12. Gangoli Rao, A., Yin, F., Werij, H.: Energy transition in aviation: the role of cryogenic fuels. *Aerospace* **7**, 181 (2020). <https://doi.org/10.3390/aerospace7120181>
13. Greitzer, E.M., Bonnefoy, P., de la Rosa Blanco, E., et al.: N+3 Aircraft Concept Designs and Trade Studies. Volume 2: Appendices - Design Methodologies for Aerodynamics, Structures, Weight, and Thermodynamic Cycles. Tech. Rep. NASA/CR-2010-216794/VOL2, National Aeronautics and Space Administration (NASA) (2010)
14. Guerreiro, A.P., Fonseca, C.M., Paquete, L.: The hypervolume indicator: computational problems and algorithms. *ACM Comput. Surv.* (2021). <https://doi.org/10.1145/3453474>
15. Henderson, R.P., Martins, J.R.R.A., Perez, R.E.: Aircraft conceptual design for optimal environmental performance. *Aeronaut. J.* (1968) **116**(1175), 1–22 (2012). <https://doi.org/10.1017/S000192400000659X>
16. Husemann, M., Schäfer, K., Stumpf, E.: Flexibility within flight operations as an evaluation criterion for preliminary aircraft design. *J. Air Transp. Manag.* **71**, 201–214 (2018). <https://doi.org/10.1016/j.jairtraman.2018.04.007>
17. Hydrogen Council: Path to Hydrogen Competitiveness: A Cost Perspective. Tech. rep. (2020). <https://hydrogencouncil.com/en/path-to-hydrogen-competitiveness-a-cost-perspective/>
18. IPCC: Climate Change 2021: The Physical Science Basis. Contribution of Working Group I to the Sixth Assessment Report of the Intergovernmental Panel on Climate Change. Cambridge University Press (2021)

19. Jenkinson, L.R., Simpkin, P., Rhodes, D.: Civil jet aircraft design. Arnold, London (1999)
20. Khandelwal, B., Karakurt, A., Sekaran, P.R., et al.: Hydrogen powered aircraft: the future of air transport. *Prog. Aerosp. Sci.* **60**, 45–59 (2013). <https://doi.org/10.1016/j.paerosci.2012.12.002>
21. Klug, H.G., Faass, R.: Cryoplane: hydrogen fuelled aircraft - status and challenges. *Air & Space Europe* **3**(3), 252–254 (2001). [https://doi.org/10.1016/S1270-0958\(01\)90110-8](https://doi.org/10.1016/S1270-0958(01)90110-8)
22. Koch, A.: Climate impact mitigation potential given by flight profile and aircraft optimization. Phd, Technischen Universität Hamburg-Harburg, Hamburg (2013)
23. Kundu, A.K.: Aircraft Design. Cambridge Aerospace Series. Cambridge University Press (2010). <https://doi.org/10.1017/CBO9780511844652>
24. Lee, D.S., Fahey, D.W., Skowron, A., et al.: The contribution of global aviation to anthropogenic climate forcing for 2000 to 2018. *Atmos. Environ.* **244**(117), 834 (2021). <https://doi.org/10.1016/j.atmosenv.2020.117834>
25. Lefebvre, A.H., Ballal, D.R.: Gas turbine combustion: alternative fuels and emissions, 3rd edn. CRC Press (2010)
26. Marek, C., Smith, T., Kundu, K.: Low emission hydrogen combustors for gas turbines using lean direct injection. In: 41st AIAA/ASME/SAE/ASEE Joint Propulsion Conference & Exhibit, (2005) <https://doi.org/10.2514/6.2005-3776>
27. Marquart, S., Ponater, M., Ström, L., et al.: An upgraded estimate of the radiative forcing of cryoplane contrails. *Meteorol. Z.* **14**, 573–582 (2005). <https://doi.org/10.1127/0941-2948/2005/0057>
28. Mason, W.: Analytic models for technology integration in aircraft design. In: Aircraft Design, Systems and Operations Conference, Dayton, OH (1990) <https://doi.org/10.2514/6.1990-3262>
29. Mattingly, J.D., Heiser, W.H., Pratt, D.T.: Aircraft Engine Design, 2nd edn. American Institute of Aeronautics and Astronautics (AIAA) (2002) <https://doi.org/10.2514/4.861444>
30. Obert, E.: Aerodynamic Design of Transport Aircraft. IOS press (2009)
31. Onorato, G., Proesmans, P., Hoogreef, M.: Assessment of hydrogen transport aircraft: Effects of fuel tank integration. *CEAS Aeronaut. J.* **13**(4), 813–845 (2022). <https://doi.org/10.1007/s13272-022-00601-6>
32. Pinho Chiozotto, G.: Improving aircraft conceptual design with methods for wing loads, aeroelasticity and mass estimation. Phd, Technischen Universität Berlin, Göttingen (2017)
33. Ponater, M., Pechtl, S., Sausen, R., et al.: Potential of the cryoplane technology to reduce aircraft climate impact: a state-of-the-art assessment. *Atmos. Environ.* **40**(36), 6928–6944 (2006). <https://doi.org/10.1016/j.atmosenv.2006.06.036>
34. Priyadarshini, M., Bhupendra, K., Vishal, S., et al.: Hydrogen as a fuel for gas turbine engines with novel micromix type combustors. In: 47th AIAA/ASME/SAE/ASEE Joint Propulsion Conference & Exhibit, San Diego, California (2011) <https://doi.org/10.2514/6.2011-5806>
35. Proesmans, P., Vos, R.: Airplane design optimization for minimal global warming impact. *J. Aircr.* **59**(5), 1363–1381 (2022). <https://doi.org/10.2514/1.C036529>
36. Roskam, J.: Airplane Design. Part I: Preliminary Sizing of Airplanes. DARcorporation(1985)
37. Roskam, J.: Airplane Design. Part VIII: Airplane Cost Estimation: Design, Development, Manufacturing and Operating. DARcorporation (1985)
38. Schumann, U.: Influence of propulsion efficiency on contrail formation. *Aerosp. Sci. Technol.* **4**(6), 391–401 (2000). [https://doi.org/10.1016/S1270-9638\(00\)01062-2](https://doi.org/10.1016/S1270-9638(00)01062-2)
39. Schwartz Dallara, E., Kroo, I.M., Waitz, I.A.: Metric for comparing lifetime average climate impact of aircraft. *AIAA J.* **49**(8), 1600–1613 (2011). <https://doi.org/10.2514/1.J050763>
40. Sethi, V.: Advanced Performance Simulation of Gas Turbine Components and Fluid Thermodynamic Properties. Phd, Cranfield University, Cranfield (2008)
41. Ström, L., Gierens, K.: First simulations of cryoplane contrails. *J. Geophys. Res.: Atmos.* **107**(D18):AAC 2–1–AAC 2–13 (2002). <https://doi.org/10.1029/2001JD000838>
42. Svensson, F., Singh, R.: Effects of using hydrogen on aero gas turbine pollutant emissions, performance and design. In: Turbo Expo: Power for Land, Sea, and Air, Vienna, pp. 107–116 (2004). <https://doi.org/10.1115/GT2004-53349>
43. Svensson, F., Hasselrot, A., Moldanova, J.: Reduced environmental impact by lowered cruise altitude for liquid hydrogen-fuelled aircraft. *Aerosp. Sci. Technol.* **8**(4), 307–320 (2004). <https://doi.org/10.1016/j.ast.2004.02.004>
44. Swelbar, W.S., Belobaba, P.P.: Airline Data Project (2019). <http://web.mit.edu/airlinedata/www/default.html>
45. Torenbeek, E.: The Initial Calculation of Range and Mission Fuel During Conceptual Design. Tech. Rep. LR-525, Delft University of Technology, Faculty of Aerospace Engineering (1987)
46. Torenbeek, E.: Synthesis of Subsonic Airplane Design. Delft University Press and Kluwer Academic Publishers, Dordrecht (1982)
47. Verstraete, D.: The Potential of Liquid Hydrogen for Long Range Aircraft Propulsion. Phd, Cranfield University, Cranfield (2009)
48. Verstraete, D.: On the energy efficiency of hydrogen-fuelled transport aircraft. *Int. J. Hydrogen Energy* **40**(23), 7388–7394 (2015). <https://doi.org/10.1016/j.ijhydene.2015.04.055>
49. Verstraete, D., Hendrick, P., Pilidis, P., et al.: Hydrogen fuel tanks for subsonic transport aircraft. *Int. J. Hydrogen Energy* **35**(20), 11,085–11,098 (2010). <https://doi.org/10.1016/j.ijhydene.2010.06.060>
50. Walsh, P.P., Fletcher, P.: Gas Turbine Performance, 2nd edn. Blackwell Science Ltd, Oxford (2004)
51. Westenberger, A.: H2 technology for commercial aircraft. In: Advances on Propulsion Technology for High-Speed Aircraft, Neuilly-sur-Seine (2008), [www.sto.nato.int/publications](http://www.sto.nato.int/publications)

**Publisher's Note** Springer Nature remains neutral with regard to jurisdictional claims in published maps and institutional affiliations.